UC Berkeley
UC Berkeley Previously Published Works

Title

Charge density waves in two-dimensional transition metal dichalcogenides

Permalink

Journal

ISSN

Authors

Hwang, Jinwoong

Ruan, Wei

Chen, Yi

et al.

Publication Date

DOI

Copyright Information

Peer reviewed

Review Article

Charge density waves in two-dimensional transition metal dichalcogenides

Jinwoong Hwang[1], Wei Ruan[2], Yi Chen[3,4,5], Shujie Tang[6], Michael F. Crommie[7,8,9], Zhi-Xun Shen[10,11], Sung-Kwan Mo[12]

[1] Department of Physics and Institute of Quantum Convergence Technology, Kangwon National University, Chuncheon 24341, Korea

[2] State Key Laboratory of Surface Physics and Department of Physics, Fudan University, Shanghai 200438, China

[3] International Center for Quantum Materials, School of Physics, Peking University, Beijing 100871, China

[4] Collaborative Innovation Center of Quantum Matter, Beijing, 100871, China

[5] Interdisciplinary Institute of Light-Element Quantum Materials and Research Center for Light-Element Advanced Materials, Peking University, Beijing 100871, China

[6] State Key Laboratory of Functional Materials for Informatics, Shanghai Institute of Microsystem and Information Technology, Chinese Academy of Sciences, Shanghai 200050, China

[7] Department of Physics, University of California, Berkeley, CA, USA

[8] Materials Sciences Division, Lawrence Berkeley National Laboratory, Berkeley, CA 94720, USA

[9] Kavli Energy NanoSciences Institute at the University of California at Berkeley, Berkeley, CA, 94720, USA

[10] Geballe Laboratory for Advanced Materials, Departments of Physics and Applied Physics, Stanford University, Stanford, CA, USA

[11] Stanford Institute for Materials and Energy Sciences, SLAC National Accelerator Laboratory, Menlo Park, CA, 94025, USA

[12] Advanced Light Source, Lawrence Berkeley National Laboratory, Berkeley, CA 94720 USA

E-mail: `jwhwang@kangwon.ac.kr`, `weiruan@fudan.edu.cn`, `yichen@pku.edu.cn`, `tangsj@mail.sim.ac.cn`, `skmo@lbl.gov`

February 2024

Abstract. Charge density wave (CDW) is one of the most ubiquitous electronic orders in quantum materials. While the essential ingredients of CDW order have been extensively studied, a comprehensive microscopic understanding is yet to be reached. Recent research efforts on the CDW phenomena in two-dimensional (2D) materials provide a new pathway toward a deeper understanding of its complexity. This review provides an overview of the CDW orders in 2D with atomically thin transition metal dichalcogenides (TMDCs) as the materials platform. We mainly focus on the electronic structure investigations on the epitaxially grown TMDC samples with angle-resolved photoemission spectroscopy and scanning tunneling microscopy/spectroscopy as complementary experimental tools. We discuss the possible origins of the 2D CDW,

novel quantum states coexisting with them, and exotic types of charge orders that can only be realized in the 2D limit.

1. Introduction

Charge density wave (CDW) is a periodic modulation in the electron density that spontaneously breaks the translational symmetry of a solid [1–6]. It occurs due to the instabilities either in the Fermi surface (FS) or lattice and gets amplified by the electron-phonon coupling. Despite the long history of research on the subject [7–10] and the ubiquitous nature of CDW orders in many quantum materials, a comprehensive microscopic understanding of CDW is yet to be reached. Nonetheless, many essential aspects of CDW transition, such as FS nesting, Kohn anomaly, strong momentum-dependent electron-phonon coupling, band Jahn-Teller effect, and excitonic interaction, have been established [1, 11], and new materials with competing electronic, magnetic, and topological orders [12–18] have been found to keep the old problem being examined with fresh perspectives.

Transition metal dichalcogenides (TMDCs), a layered material family with a transition metal layer sandwiched by two chalcogen (S, Se, Te) layers, have been a model system in studying CDW orders [4, 19]. They stabilize in various structural phases following the relative orientation of layer stacking, and the electronic structure modification caused by the structural and elemental changes brings about substantial differences in the nature of CDW order [4,20]. The recent development of thinning down the TMDC materials to atomically thin two-dimensional (2D) limit to harness material properties vastly different from those of bulk [20–24] has sparked renewed interest in the various CDW phases of TMDCs in atomically thin, few-layer form. Several interesting questions naturally arise when symmetry changes and the quantum confinement effect becomes prominent in the few-layer TMDCs: (i) What happens to the CDW order itself? Would it retain the same ordering vector as in bulk? How about the transition temperature? (ii) If there is any change in the CDW order in the 2D limit, how would it affect the coexisting orders, for example, superconductivity? (iii) Can any novel quantum many-body phenomena emerge alongside the CDW order? (iv) How would the reduced screening and subsequent increase in electron-electron and electron-hole interaction affect the CDW transition? (v) Can there be any novel CDW phases, hard to find in bulk, favored in the reduced dimensionality?

In this review, we summarize the recent research efforts to answer these questions by investigating the electronic structures of few-layer TMDCs. We particularly focus on the results from two complementary experimental tools to study the electronic properties of solid, angle-resolved photoemission spectroscopy (ARPES) and scanning tunneling microscopy/spectroscopy (STM/STS). We also focus on the atomically thin samples synthesized by molecular beam epitaxy (MBE). Still, other samples from standard preparation methods, such as exfoliation and chemical vapor deposition (CVD), will be discussed.

Below, we first briefly discuss the basic concepts of CDW transition and introduce the experimental and theoretical techniques in relation to the CDW. Then, we organize subsequent sections by TMDC materials that are representative of the aforementioned

research questions.

1.1. Basic concepts of charge density waves

Many key concepts of CDW transition are well captured in the Peierls transition of the 1D weakly interacting metallic chain [1, 8]. The Lindhard susceptibility $\chi_L(\mathbf{q})$, which connects electro-static perturbation $\phi(\mathbf{q})$ to the induced charge $\rho^{\text{ind}}(\mathbf{q})$ through the linear response equation $\rho^{\text{ind}}(\mathbf{q}) = \chi_L(\mathbf{q})\phi(\mathbf{q})$, diverges in 1D (Fig. 1(a)). This divergence is due to the "nesting" property of the 1D FS (Fig. 1(b)), i.e., two points in the FS are connected by a common wave vector $q = 2k_F$, consequently making the denominator of $\chi_L(\mathbf{q})$ zero. The diverging χ_L implies that any small perturbation will lead to a huge charge redistribution at $T = 0$, i.e., the electron system is unstable (Peierls instability). At a finite temperature, the thermal broadening weakens the divergence. However, χ_L is still large at low temperatures [1], making CDW formation possible below a certain transition temperature $T < T_{\text{CDW}}$ for a given system.

When the charge redistribution occurs, the lattice responds through electron-phonon interaction to compensate for the increased Coulomb repulsion in the charge
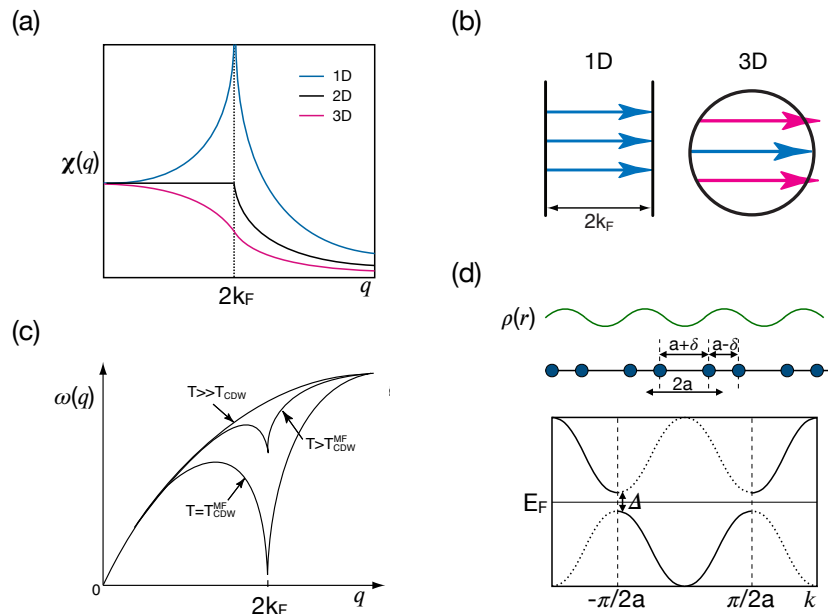

Figure 1. Basic concepts of charge density wave (a) Lindhard susceptibility for weakly interacting electrons in different dimensions. (b) A perfect nesting in the Fermi surface of free electron-like 1D electrons. Imperfect nesting in a sphere-shaped Fermi surface of 3D electrons. (c) Phonon dispersion relation from the mean-field solution of 1D Fröhlich Hamiltonian. (d) Schematic diagram of the CDW formation due to Peierls instability in a 1D chain. $\rho(r)$ is the electron density along the 1D chain. The bottom panel shows the electron energy-momentum dispersion relation. Δ is the CDW gap. The curves in solid lines are the gapped original bands, and the ones in dotted lines are the folded bands. Figures are created by the authors taking Refs. [1, 2, 4–6, 11] as references.

channel. An insightful picture can be gained, e.g., from the mean-field solution of Fröhlich Hamiltonian [1, 7] (Fig. 1(c)). The phonon frequency is significantly reduced near $q = 2k_F$, especially for low-T and 1D (phonon softening). This is a direct consequence of electron-phonon interaction and divergent χ_L, referred to as the Kohn anomaly. The temperature at which the phonon frequency becomes zero defines the transition temperature, T_{CDW}, indicating a "frozen-in" lattice distortion.

The overall consequences of the instabilities in both electron density and lattice are represented schematically in Fig. 1(d). The periodic lattice distortion (PLD) opens a gap at the Fermi energy (E_F) to compensate for the increased Coulomb repulsion and elastic energy. The doubling of the lattice results in the periodic modulation in the electron density following the new periodicity. In the reciprocal space, the base vector becomes half its original value, and the electron bands are "folded" into the new periodicity in the extended zone scheme. As we discuss more in the following subsection, the real space modulation of electron density is naturally detected by STM, while ARPES has been essential in discerning the opening of a gap and the band folding in the reciprocal space.

While Peierls instability and the nesting picture capture the essential features of CDW, such as phonon softening, gap opening, and band folding, the realistic description of CDW phenomena beyond simple metallic 1D chain is hard to obtain and heavily material specific. While FS nesting still explains some features of CDW formation in 2D layered materials [25, 26], it does not fully account for the CDWs in many 2D and 3D materials. Prime examples are TMDCs [4, 6, 11]. It has been widely suggested that a strong **q**-dependent electron-phonon coupling can create phonon softening and subsequent PLD and CDW [27–29]. The particular band topology of TMDCs allows a logarithmic divergence of Lindhard susceptibility at the momentum connecting saddle points below Fermi energy [30], which has been proposed to explain the lack of FS nesting in $2H$-NbSe$_2$ and $2H$-TaSe$_2$. Another notable mechanism of CDW in TMDCs includes the idea of an excitonic insulator, in which the formation of CDW is associated with the spontaneous formation of an exciton condensate in small-gap semiconductors and semimetals [31, 32].

1.2. Experimental and theoretical probes for CDW

The physical properties associated with the CDW transition, e.g., PLD, opening of a gap, and FS reconstruction, can be measured by various experimental probes. The opening of a gap shows up in transport measurements as a "CDW hump" in the temperature-dependent resistivity curves [2, 10, 33]. Spectroscopic tools, including optical conductivity, STS, and ARPES, can measure the size of the gap directly [25, 34–37]. The FS reconstruction can be seen through quantum oscillation and ARPES measurements [38–40]. The PLD and the breaking of translational symmetry would be measured by x-ray scattering, electron diffraction, STM, and NMR measurements [13, 14, 41–46]. Raman scattering reveals phonon softening and the

appearance of amplitude mode [47, 48]. The Kohn anomaly can also be measured by the inelastic neutron and x-ray scattering [29, 49, 50]. The second-order phase transition nature of CDW transition results in anomalies in the thermodynamic measurements, such as specific heat [51]. This review primarily focuses on the ARPES and STM/STS, which provide complementary views on the gap opening, electronic band and FS reconstruction, and periodic modulation in the electron density and lattice.

ARPES has become a standard tool to study CDW or any other collective many-body phenomena by directly measuring the momentum-resolved electronic structure of quantum materials [52–54]. It can provide information not only on the size of the CDW gap, but also on the exact momentum and energy position of the gap in the reciprocal space with the temperature evolution of the gap size [25, 39, 40, 55–57]. ARPES also directly measures the electron band structure, and its folding due to the PLD and the formation of the superstructure, enabling a direct comparison to the advanced theoretical calculations [37, 39, 40, 58]. Since photoemission is a hybrid of spectroscopy and scattering experiments, the details of lineshape, spectral weight distribution, and spectral weight transfer, all carry important information related to the underlying mechanism of quantum phases [57, 59–61]. We will later see that the ARPES results from CDW systems are no exception. All this information from ARPES has been proven to be crucial in investigating the driving mechanism and the nature of the CDW phases, and in setting up the baseline for the more advanced experimental and theoretical studies.

While ARPES probes momentum-dependent spectral function by extracting electrons at well-defined crystal momentum from a sample, STM extracts or injects electrons at well-defined real-space positions. This is achieved through quantum tunneling between the sample and a tip, by which STM detects the local density of states (LDOS) of electrons, a quantity that essentially characterizes how many possible states a sample has for electron extraction or injection at the given tip position at a given energy [62, 63]. Complimentary to the information provided by ARPES, STM-based techniques have four unique advantages in characterizing a CDW state. First, because of the close relationship between LDOS and charge density, atomic-scale STM imaging allows direct visualization of charge-density modulation (the CDW order parameter) [45, 64]. For example, temperature-dependent STM imaging can tell us how charge-density modulation diminishes beyond T_{CDW}. Second, STM/STS can probe both occupied and unoccupied states of a sample. This is particularly useful when the energy position of the CDW gap is above the E_{F} [65]. Third, the energy resolution of STM/STS is typically only limited by thermal broadening and can reach a sub-meV level in modern cryogenic systems. Because of the last two features, STM is particularly suitable for resolving fine CDW gaps in many CDW systems [66]. Last, spectroscopic information obtained by STS can be correlated with real-space information obtained by STM, providing a unique method to characterize electronic structure associated with CDW variations, domain walls, defects, and other CDW-related local 0D or 1D features [67–70].

Throughout this review, the ARPES and STM results are closely compared to theoretical calculations, particularly density functional theory (DFT) and its variants [71–74]. While some of the essential features of the CDW ordering in TMDCs may be captured in a more simplistic theoretical approaches [4], DFT has been the go-to theoretical tool to investigate the microscopic origin of CDW orders by providing information on the crystal structure, phonon softening, electronic band structure, Fermi surface topology, and energy gap [6, 11, 27, 28, 74]. Despite being a powerful and widely used theoretical method, DFT has its shortcomings in, e.g., estimating the size of the gap, and including van der Waals (vdW) interaction, non-local interaction, and electron correlation [71–73], which are all relevant in understanding the CDW and surrounding quantum phases as will be discussed in more detail below. New and improved computational methods continue to be developed to overcome such shortcomings, including devising complex hybrid functionals [72], the inclusion of on-site Coulomb interaction (DFT+U) [75], and applying a machine learning approach to the DFT calculations [76].

2. CDW phases in two-dimensional TMDCs

In this section, we review works regarding the properties and driving mechanisms of CDW phases in single-layer $1H$-NbSe$_2$/TaSe$_2$, $1T$-VSe$_2$/VTe$_2$, and $1T$-TiSe$_2$/TiTe$_2$. Owing to their complexity and novelty, we defer the discussion of single-layer $1T$-TaSe$_2$, $1T$-ZrTe$_2$, and $1T$-IrTe$_2$/TaTe$_2$ to dedicated later sections.

2.1. Persistent 3×3 CDW orders in 1H-NbSe$_2$ and 1H-TaSe$_2$

Bulk $2H$-NbSe$_2$ has long been studied as a prototypical CDW system in which the interaction of superconductivity (SC) and CDW orders is most pronounced [19, 77]. It hosts CDW with $T_{\mathrm{CDW}} \sim 33$ K and SC with $T_C = 7.2$ K. In the quasi-2D FS, the nesting condition is far from ideal [11], therefore strong momentum-dependent electron-phonon coupling has been proposed as a driving mechanism of CDW in $2H$-NbSe$_2$ [11,28,29,57]. However, a coherent understanding of the CDW mechanism here is still lacking, partially due to the complexity involved in its electronic structure [4, 78–80]. This motivates the investigation of $2H$-NbSe$_2$ in atomically thin monolayer (ML) limit, where a simplified low-energy electronic structure is expected in the absence of interlayer coupling [81]. This may help us discern the competing or cooperating CDW and SC orders.

Monolayer $1H$-NbSe$_2$ has been grown by MBE on a bilayer graphene (BLG) substrate [82]. The existence of two-dimensional CDW is directly established through atomically-resolved STM imaging, as shown in Fig. 2. The periodicity of the CDW wavevector is confirmed to be $\sim 3{\times}3$ with $\mathbf{q}_{\mathrm{CDW}} = (\frac{1}{3}\ \frac{1}{3}\ 0)\mathrm{R}0°$ r.l.u. (reciprocal lattice unit; the number after R is the angle between the original reciprocal lattice vector and the $\mathbf{q}_{\mathrm{CDW}}$) by the Fourier transform of STM image, which is similar to previous STM measurements of bulk $2H$-NbSe$_2$ [44,83]. The CDW of ML $1H$-NbSe$_2$ weakens at an

elevated temperature $T = 25$ K, where patches of CDW are seen to be separated by regions without CDW. At $T = 45$ K, no 3×3 charge modulations can be observed. Given that bulk $2H$-NbSe$_2$ has $T_{CDW} \sim 35$ K, this suggests that single-layer and bulk NbSe$_2$ have similar CDW strength. The overall electronic structure measured from STS and ARPES is consistent with each other. The polarization-dependent ARPES finds a much simplied band structure than the bulk, highlighted by the single band crossing the E_F (Fig. 2) [82].

The existence of a similar 3×3 CDW in single-layer $1H$-NbSe$_2$ despite the simplified low energy band structure (Fig. 2) and FS topology allows us to draw some conclusions regarding the mechanism of CDW formation. First, we may rule out some of the proposed dimensionality effects on the CDW phase of ML $1H$-NbSe$_2$, e.g., reduction of the CDW wavevector in the 2D limit [81]. Second, the inner pockets around Γ and K in the bulk $2H$-NbSe$_2$ electronic structure are most likely not crucial for the CDW formation as these bands are not present in the ML while the CDW remains mostly unchanged. Based on this observation, we may rule out proposed FS nesting mechanisms involving these pockets [57, 78, 84]. The absence of these pockets in single-layer $1H$-NbSe$_2$ makes the geometric nesting condition of the FS more difficult to achieve and favors a CDW mechanism driven by electron-phonon coupling [11, 47].

While the 3×3 CDW order persists in ML with roughly the same transition temperature, the superconducting T_C gets suppressed heavily down to ~ 2 K [82, 85, 86]. Optical measurements on exfoliated ML $1H$-NbSe$_2$ [86] find essentially the same suppression of SC while it reports an increase in the T_{CDW}, which raised the issue of sample quality and the impurity pinning [1, 87]. The superconductivity in $1H$-NbSe$_2$ has been further discussed in terms of multifractal [88] and 2D Ising SC [89]. The electronic structure of $1H$-NbSe$_2$ on BLG has been successfully reproduced even with the MBE-grown samples on various other substrates [90–92]. At the same time, Dreher *et al.* find that some of the substrates strongly interacting with the NbSe$_2$ layer, e.g., Au(111) or $2H$-WSe$_2$, can destroy either or both CDW and SC order.

$2H$-TaSe$_2$ provides an ideal testbed for a comparative CDW study against $2H$-NbSe$_2$ since SC in this system is largely suppressed with $T_C \sim 0.2$ K even in the bulk [93]. The combined STM and ARPES measurements on the MBE-grown $1H$-TaSe$_2$ find 3×3 CDW order persists down to ML despite the low-energy electronic band structure and FS topology becomes much simpler, similar to the $1H$-NbSe$_2$ case [94]. The STM measurements establish the CDW ordering vector as $\mathbf{q}_{CDW} = 2/3\ \Gamma M$. ARPES measurements reveal that upon the formation of CDW, the FS becomes gapped mainly at the momenta equivalent to $\mathbf{q}_{CDW}$ with a gap size reaching ~ 100 meV. The CDW gap closes at $T \sim 130$ K with increasing temperature, defining the CDW transition temperature. The T_{CDW} of ML $1H$-TaSe$_2$ shows only a slight increase from its bulk value ~ 122 K [95, 96]. Comparison with the first principles calculation finds that enhanced spin-orbit coupling and lattice distortion play a crucial role in the formation of CDW order, and suggest that the strong momentum-dependent electron-phonon coupling is a likely driving mechanism of the CDW order in ML $1H$-TaSe$_2$ [47, 94].

Material	Normal	1st CDW	2nd CDW	3rd CDW
$2H$-NbSe$_2$	$T > 33$ K	$T < 33$ K		
Ref. [77]	Normal	IC $\sim 3 \times 3$		
$2H$-TaSe$_2$	$T > 122$ K	90 K $< T <$ 122 K	$T < 90$ K	
Ref. [77]	Normal	IC $\sim 3 \times 3$	C 3×3	
$2H$-TaS$_2$	$T > 75$ K	$T < 75$ K		
Ref. [96]	Normal	IC $\sim 3 \times 3$		
$1T$-TaSe$_2$	$T > 600$ K	473 K $< T <$ 600 K	$T < 473$ K	
Ref. [19]	Normal	IC $\sim 3.6 \times 3.6$	C$\sqrt{13} \times \sqrt{13}$R13.9°	
$1T$-TaS$_2$	$T > 543$ K	353 K $< T <$ 543 K	See caption	$T < 183$ K
Ref. [141]	Normal	IC $\sim 3.5 \times 3.5$	NC + T	C$\sqrt{13} \times \sqrt{13}$R13.9°
$1T$-TiSe$_2$	$T > 202$ K	$T < 202$ K		
Ref. [118]	Normal	C $2 \times 2 \times 2$		
$1T$-VSe$_2$	$T > 110$ K	$T < 110$ K		
Ref. [97]	Normal	IC $4 \times 4 \times \sim 3.2$		

Table 1. Charge density waves of bulk transition metal dichalcogenides. In this table, "C" and "IC" refer to a commensurate and an incommensurate CDW, respectively. Following the convention, CDW periodicities are described relative to the undistorted atomic lattice periodicities, where "R" indicates a nonzero rotation angle between the two lattices. For $1T$-TaS$_2$, the CDW behavior at the intermediate temperature range is complicated. Upon cooling, a so-called near-commensurate (NC) CDW phase with periodicity $\sim 3.5 \times 3.5$R11-13° occurs at 183 K $< T <$ 353 K. Upon warming, a triclinic (T) CDW phase first appears 223 K $< T <$ 280 K, above which the NC CDW phase appears at 280 K $< T <$ 353 K [141].

2.2. 2D Fermi surface nesting driven CDW transition in 1T-VSe$_2$ and 1T-VTe$_2$

$1T$-VSe$_2$ has been of particular interest in the TMDC family due to its unusually long wavelength 3D CDW order in the bulk. A PLD in bulk $1T$-VSe$_2$ was reported in x-ray and electron-diffraction measurements below $T_{\text{CDW}} \sim 110$ K, and the CDW vector has both commensurate in-plane and incommensurate out-of-plane components $4 \times 4 \times 3.2$ with $\mathbf{q}_{\text{CDW}} \approx (\frac{1}{4}\ \frac{1}{4}\ \frac{1}{3})$R0° r.l.u. [19,97–99], suggesting 3D characteristics despite the layered crystal structure. More interestingly, $1T$-VSe$_2$ has ellipse-shaped electron pockets centered at M(L) that follow the threefold symmetry of the Brillouin zone (BZ) interior, where the two long sides of each elliptical pocket at M are almost straight and nearly parallel [100–102]. This FS topology offers an excellent nesting condition, and the nesting vector is closely matched with the CDW vector, suggesting the FS nesting as a mechanism for the CDW transition [100,103]. Indeed, a soft x-ray ARPES study on bulk $1T$-VSe$_2$ showed the FS measurement including k_z and the possible existence of a 3D FS nesting vector [100]. However, the 3D FS nesting picture is still under controversy since detailed ARPES studies claimed that the FS nesting picture is not suitable due to the 3D warping effect and the absence of the CDW gap at any point of the BZ in bulk $1T$-VSe$_2$ [101,102]. Instead, the momentum dependence of the strong electron-phonon
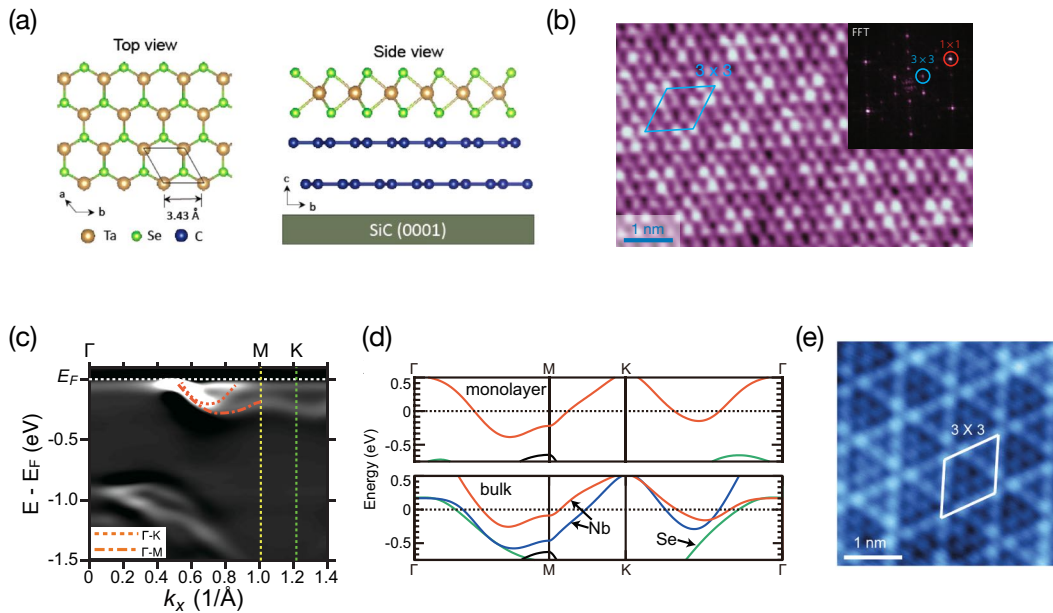
Figure 2. Charge density wave in single-layer $1H$-NbSe$_2$ and $1H$-TaSe$_2$ (a) Top and side views of $1H$-NbSe$_2$ and $1H$-TaSe$_2$ samples grown on bilayer graphene/SiC substrates by MBE. (b) 3×3 CDW structure of $1H$-NbSe$_2$ imaged by STM. The inset shows the Fourier transform of the image with the primary and 3×3 superstructure peaks. (c) ARPES intensity map of $1H$-NbSe$_2$. Due to the rotational degeneracy of the epitaxially grown samples, the ARPES signals along Γ-M and Γ-K directions overlap in a single detection angle. (d) DFT band calculation results of bulk and single-layer $1H$-NbSe$_2$. The band structure is significantly simplified in single-layer $1H$-NbSe$_2$, but the 3×3 CDW still persists. (e) Intensity modulation due to 3×3 CDW in the STM image of $1H$-TaSe$_2$. Figures are reproduced from Refs. [82, 94]

coupling is suggested as a primary driving mechanism in bulk $1T$-VSe$_2$, supported by inelastic x-ray scattering [104] and Raman studies [105], due to the dominant role of vdW interactions.

Thinned down to an atomically thin 2D limit, CDW order and driving mechanism can be modified due to the change of the electronic structure as well as the absence of the k_z dispersion [101,106–110]. Indeed, the epitaxially grown ML $1T$-VSe$_2$ exhibits $\sqrt{7}\times\sqrt{3}$ CDW, $\mathbf{q}_{\text{CDW}} = (\frac{1}{\sqrt{7}}\ \frac{1}{\sqrt{3}}\ 0)$R11° r.l.u. [109], in contrast to the 4×4 for the bulk. The change of the CDW vector is due to the formation of the perfect 2D FS nesting condition driven by enhanced electron-electron correlations in ML $1T$-VSe$_2$ [106,111]. Moreover, the CDW gap is clearly obtained in ML $1T$-VSe$_2$ at perfectly nested FS sections with gap size $60 \sim 90$ meV, suggesting the FS nesting picture as a CDW driving mechanism in ML $1T$-VSe$_2$ [101,106–109].

Despite the clear signature of the CDW superstructure and gap in ML $1T$-VSe$_2$, discrepancies exist in determining the T_{CDW}. While low energy electron diffraction (LEED) [107] and STM measurements [106, 109] extracted $T_{\text{CDW}} = 140$ - 150 K, the ARPES results show a very broad range of $T_{\text{CDW}} = 110$ - 340 K by fitting the

temperature-dependence of CDW gap to a BCS model [101,106,109]. Moreover, ARPES reveals an anisotropic two-gap structure in ML $1T$-VSe$_2$, where the band near Γ starts opening the gap below ~ 150 K while another band near M shows a two-step transition of the gaps at 150 K and 340 K, respectively [109]. Since the $\sqrt{7}\times\sqrt{3}$ CDW superstructure is only obtained below 150 K, several possible origins of the high-temperature gap structure have been proposed, including the substrate effect [106], pseudogap phase by charge and spin fluctuation [108], and hidden incommensurate CDW formation at high temperature [109].

The unique $\sqrt{7}\times\sqrt{3}$ CDW and the two-gap structures obtained in ML totally disappear even at the bilayer (BL) thickness. BL $1T$-VSe$_2$ film exhibits 4×4 CDW like the bulk case, albeit without ordering in the k_z direction, and $T_{\text{CDW}} \sim 180$ K, much higher than the bulk value of 110 K [110]. As thickness increases, 4×4 CDW order persists and T_{CDW} is suppressed. Since the additional layers modify the FS topology due to the relaxed quantum confinement, resulting in the transition from $\sqrt{7}\times\sqrt{3}$ to 4×4 CDW formations, the thickness-dependent behaviors in $1T$-VSe$_2$ are understood in terms of the dimensional crossover of phonon instability driven by competition of nesting vectors [110]. Therefore, the FS nesting picture is considered as a fundamental driver for the CDW transition in epitaxially grown $1T$-VSe$_2$ films, which leads to first-order energy lowering following the PLD in accordance with the nesting conditions [101, 106, 110].

Another FS nesting-driven CDW material in TMDC is ML $1T$-VTe$_2$ [112–114], a sister compound of $1T$-VSe$_2$. Bulk $1T$-VTe$_2$ has been reported to have a $3\times1\times3$ CDW order with $T_{\text{CDW}} = 480$ K, and FS shows a quasi-1D character due to the formation of V double zigzag chain by the strong Te-Te interlayer coupling and Jahn-Teller distortion [115–117]. In the ML limit, where the total absence of the Te-Te interlayer coupling, the FS significantly changes from that of bulk, and it becomes similar to that of $1T$-VSe$_2$ with well-defined 4×4 nesting condition along the M-K direction [112,113]. Both ML films display a similar triangular pocket at the K point, whereas a circular hole pocket only exists in $1T$-VSe$_2$ [112]. The CDW ordering vector of ML $1T$-VTe$_2$ is much smaller ($\mathbf{q}_{\text{CDW}} = (\frac{1}{4}\,\frac{1}{4}\,0)$R0° r.l.u.) than that of ML $1T$-VSe$_2$ due to the larger triangular pocket at the K point. LEED, STM, and ARPES measurements confirmed 4×4 CDW order in ML $1T$-VTe$_2$ with $T_{\text{CDW}} \sim 190$ K [112,113]. The CDW gap is obtained in ML $1T$-VTe$_2$ at perfectly nested FS sections with gap size ~ 50 meV [112,113], suggesting the FS nesting picture as a primary driving mechanism like ML $1T$-VSe$_2$.

2.3. TiSe$_2$, TiTe$_2$: the role of substrate

$1T$-TiSe$_2$ is a prototype of CDW materials, which has been extensively studied for decades [118]. However, the origin of the CDW state in $1T$-TiSe$_2$ is still under debate. While it is generally considered a prime candidate for an excitonic insulator with finite momentum transfer [4,32,61,119–121], a clear-cut consensus has not been reached since the resultant CDW phase and PLD is hard to discern between the electronically driven excitonic insulator and the conventional CDW. The successful epitaxial growth of ML

$1T$-TiSe$_2$ has allowed the control of the dimensionality of this material [122–125], which inspires new experimental and theoretical investigations on the origin of the CDW transition [126–129].

In the normal state of single-layer $1T$-TiSe$_2$, the bands near the Fermi level consist of a valence band centered at the Γ point, mainly derived from Se $4p$ orbits, and a conduction band centered at the M point, primarily composed of Ti $3d$ orbits. At low temperatures, the 2×2 CDW state with $\mathbf{q}_{\mathrm{CDW}} = (\frac{1}{2} \, \frac{1}{2} \, 0) \mathrm{R}0°$ r.l.u. emerges, and folding of the BZ, the conduction band, and the valence bands are observed with a CDW ordering vector that connects the Γ and M points in the $\mathbf{k}$-space. The CDW interaction further hybridizes the conduction and valence band, which opens the CDW gaps between them.

The first single-layer $1T$-TiSe$_2$ samples were grown on bilayer graphene/SiC [122, 123]. The CDW state is preserved in the ML limit, as evidenced by the folding of the top valence bands to the M point in the 2×2 superstructure. The CDW gap is found to be approximately 180 meV, much larger than the 110 meV gap in bulk $1T$-TiSe$_2$. The temperature dependence of the ML CDW gap follows a BCS-like form, yielding a transition temperature of 232 ± 5 K, slightly elevated from that of bulk. Both the increased gap size and transition temperature indicate an enhancement of the CDW instability in the 2D limit.

The thickness dependence of the CDW transition has also been studied by Raman spectroscopy on exfoliated nanoflakes of $1T$-TiSe$_2$ [130]. By tracking the evolution of the amplitude mode, the Raman measurements find that the CDW transition temperature increases as the thickness is reduced down to the ML limit, consistent with previous ARPES experiments on epitaxial $1T$-TiSe$_2$. However, the study also demonstrated the significant role of the substrate. On SiO$_2$ substrates, T_{CDW} decreases as the $1T$-TiSe$_2$ thickness is reduced. In contrast, for TiSe$_2$ encapsulated in hexagonal boron nitride (hBN), T_{CDW} increases with decreasing thickness. Remarkably, a 10 nm $1T$-TiSe$_2$ flake encapsulated in hBN exhibits an enhanced T_{CDW} up to 235K. These observations highlight that the CDW instability in few-layer $1T$-TiSe$_2$ is very sensitive to the dielectric environment, which can tune the interactions underpinning the ordered state. Careful consideration of substrate effects and dielectric screening is required to reveal the intrinsic behavior in the 2D limit.

The substrate-dependence of the CDW transition in monolayer $1T$-TiSe$_2$ has been further investigated by growing samples on different substrates and characterizing them using STM and ARPES [131, 132]. A substantial enhancement of both the CDW transition temperature and gap size is observed for $1T$-TiSe$_2$ grown on MoS$_2$ compared to graphite or graphene substrates. Remarkably, monolayer $1T$-TiSe$_2$ on MoS$_2$ exhibits an enlarged CDW gap of 250 meV and a transition temperature of 280K. These studies have shown a consistent trend that reducing the dimensionality and choosing a substrate with poorer screening strengthen the CDW in $1T$-TiSe$_2$. This aligns with theoretical expectations that the exciton binding energy increases in 2D monolayers and is highly sensitive to the dielectric environment [133–135]. The experimental enhancement of the CDW instability with lower dimensions and reduced screening lends an interesting
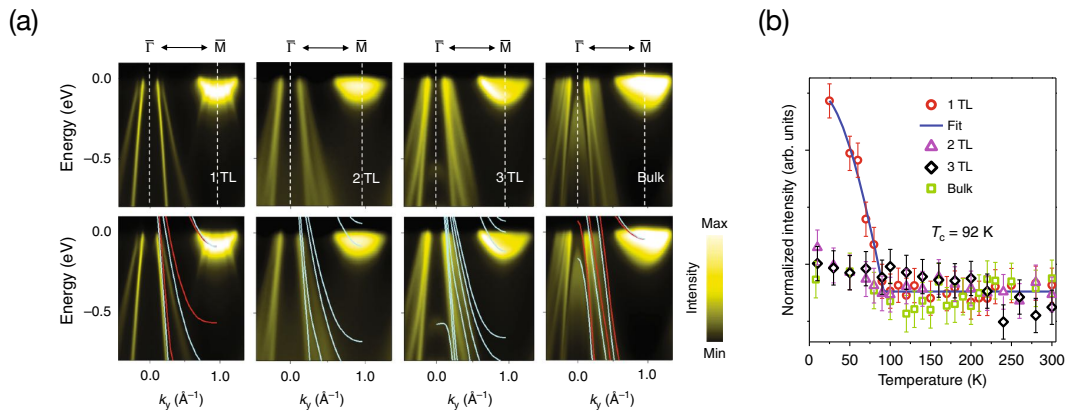
Figure 3. Layer thickness dependence of electronic band structure and CDW gap in 1T-TiTe$_2$ (a) ARPES intensity map measured along Γ-M direction for one, two, three layers, and bulk 1T-TiTe$_2$. The bottom panels are overlaid with theoretical calculations using GGA (red curves) and GGA + U (cyan curves). (b) Temperature dependence of integrated ARPES intensity in the region of folded bands around the M point. Figures are reproduced from Refs. [136]

implication for an excitonic condensation scenario as the mechanism driving the CDW in 1T-TiSe$_2$ [61, 120, 121].

1T-TiTe$_2$, a sister material of 1T-TiSe$_2$, has also been grown epitaxially in the ML limit [136–139]. Surprisingly, a 2×2 CDW was observed in ML 1T-TiTe$_2$ with a transition temperature of 92K (Fig. 3). In contrast, no CDW transition was detected in the bilayer, trilayer, or bulk 1T-TiTe$_2$, even though 1T-TiTe$_2$ is considered as quasi-2D in the bulk form (Fig. 3). Through extensive ARPES studies, evidence of band hybridization between the backfolded conduction and valence bands at the CDW transition was found [136, 139]. This hybridization gains energy by opening up the CDW gap. It was also found that the hybridization is orbital-selective, which explains the absence of the CDW state in the bulk. In the bulk, 3D band dispersions and an orbital inversion with k_z lead to mismatched backfolded bands between electron and hole pockets. This suppresses the energy gain from hybridization, explaining the lack of a CDW in bulk 1T-TiTe$_2$.

The strain also plays a vital role in enhancing or suppressing the CDW state. Zhao *et al.* found that the moir pattern formed between 1T-TiTe$_2$/1T-TiSe$_2$ with a small twist angle could raise the CDW transition temperature to above room temperature [140]. This is much higher than the CDW temperature of individual 1T-TiTe$_2$ and 1T-TiSe$_2$ layers. Fragkos *et al.* find that the epitaxial strain imposed by the InAs substrate, which compresses the 1T-TiTe$_2$ film out-of-plane and reduces the van der Waals gap between layers, enhances interlayer coupling and facilitates propagation of the CDW-driving phonon modes [137]. This allows the multilayer 1T-TiTe$_2$ films to exhibit a robust 2×2×2 CDW distortion at room temperature, unlike bulk 1T-TiTe$_2$. Lin et al. investigated the CDW state in single-layer 1T-TiTe$_2$ grown on thin films of PtTe$_2$ [138].

They found that CDW transition temperature reduces to 65K and completely suppressed in 2 or more layers of $PtTe_2$ as metallicity of $PtTe_2$ layer and screening from the substrate increases.

3. Mott insulator phase and signatures of quantum spin liquid in $1T$-TaSe$_2$ and related materials

3.1. Bulk 1T-TaS₂ and 1T-TaSe₂: history and debate

In their bulk forms, $1T$-TaS$_2$ and $1T$-TaSe$_2$ have long been known to undergo several CDW transitions upon lowering the temperature (Table 1) [19, 141]. At the lowest temperature, a commensurate in-plane $\sqrt{13} \times \sqrt{13}$ CDW with $\mathbf{q}_{CDW} = (\frac{1}{\sqrt{13}} \ \frac{1}{\sqrt{13}} \ 0)R13.9°$ r.l.u. sets in for both materials, where every 13 Ta atoms, together with 26 Se atoms around them, move closer to form a so-called star-of-David CDW cell (Fig. 4(a)). This $\sqrt{13} \times \sqrt{13}$ CDW structure is home to various predicted and reported exotic correlation behaviors, as we discuss in this section.

The unusual electronic structure of bulk $1T$-TaS$_2$ has already triggered interest in the 1970s [19, 142]. In terms of electron-number counting, each Ta^{4+} atom contributes one conduction electron, hence each star-of-David CDW unit cell contains an odd number of 13 electrons. These electrons should fill up six and a half bands, creating a metallic state at the single-particle level. In contrast to this single-particle prediction, clear insulating behavior has been shown in transport measurements of bulk $1T$-TaS$_2$ [19, 143]. Even for metallic bulk $1T$-TaSe$_2$ [19] which seemingly agrees with this prediction, the majority of its surface state has been known to be insulating [144, 145].

Two sets of ideas were proposed to resolve this apparent contradiction. The first, initially put forward by Tosatti and Fazekas in 1976 [142, 146], resorts to Mott localization [147]. It has been known that for a half-filled band with bandwidth W, a sufficiently strong Coulomb repulsion U can produce an insulating phase. As the U/W ratio increases beyond a critical value, the metal makes a transition into a Mott insulator, characterized by two Hubbard subbands separated by U [147, 148]. The early proposal of a possible Mott insulating phase in bulk $1T$-TaS$_2$ was further supported by later electronic structure calculations, which show the appearance of a half-filled flat band (i.e., with a small bandwidth W and hence a large U/W ratio) at least in the single-layer form of $1T$-TaSe$_2$ and $1T$-TaS$_2$ in the $\sqrt{13} \times \sqrt{13}$ CDW phase [149–152]. This narrow band arises in this CDW phase because the band is mainly composed of a Ta d_{z^2} orbital near the center of each CDW cell, and hence two nearest neighbors of such orbitals, separated by one superlattice constant ($\sim$1.2 nm) away from each other, experience much reduced hopping amplitude.

In a Mott insulator, each lattice site has one localized electron that carries an electron spin-1/2, and thus a Mott insulator naturally realizes a spin-1/2 lattice. Furthermore, since the CDW lattice of bulk $1T$-TaS$_2$ is triangular, the magnetic ground state is expected to be frustrated, which has been noted early on [146]. Based on

a Mott-insulating ground state and other experimental observations, Law and Lee in 2017 proposed that bulk $1T$-TaS_2 could realize a gapless quantum spin liquid (QSL) with a spinon FS [153, 154]. Some experimental evidence has been obtained [155–157], although a consensus has not been reached [150].

Recently, a second set of ideas emerged that challenges the long-held interpretation of Mott localization in bulk $1T$-TaS_2. Here, the focus was on the out-of-plane stacking of the $\sqrt{13} \times \sqrt{13}$ CDW structure [158–160], whose ramifications had not been quite thoroughly investigated (see, however, Ref. [161]). It was shown both experimentally [162–164] and theoretically [158–160, 165] that star-of-David CDW cells in bulk $1T$-TaS_2 tend to form an interlayer dimer-stacked structure, at least when sufficiently relaxed into the structural ground state [160]. As a result, in terms of electron-number counting, a CDW unit cell composed of two (vertically aligned) star-of-David cells contains an even number of 26 electrons, which makes it plausible to realize a "trivial" band insulator without invoking any strong correlation effects. A further careful comparison between the DFT bands of band-insulator electronic structure and ARPES results of bulk $1T$-TaS_2 show apparent similarities [158, 159, 165]. If the system were a band insulator, no spin liquid state would be formed.

3.2. Mott insulating state in single-layer $1T$-$TaSe_2$, $1T$-TaS_2, and $1T$-$NbSe_2$

Whether bulk $1T$-TaS_2 and $1T$-$TaSe_2$ realize a Mott insulator or a band insulator is still debated. To resolve this issue, researchers have been exploiting at least four different strategies:

(i) Sub-surface stacking. The idea is that as-grown or perturbed samples can host different stacking orders, and a careful study of them may help distinguish the contributions from interlayer coupling (which changes with stacking orders) and electron correlation (which barely changes). Indeed, in bulk $1T$-TaS_2, two distinct types of surface states of two different gap sizes have been identified [166–169]. Although the surface states with larger/smaller bandgaps have been suggested to arise from interlayer dimerization/Coulomb repulsion U, respectively [165, 166], a recent study shows that the surface electronic structure is not solely determined by the stacking of the top two CDW layers [169]. A similar complication was observed at bulk $1T$-$TaSe_2$ surface [170], where the surface states can even range from insulating to weakly metallic to strongly metallic [170, 171]. These complications create difficulty in reaching a one-to-one correspondence between stacking orders and electronic structures in related materials.

(ii) Surface modification, including adatoms [168, 172–176] or domain wall formation [177–181]. The idea is that Mott insulators and band insulators may respond to these surface modifications differently. For example, potassium (K) doping is argued to distinguish two surface states of bulk $1T$-$TaSe_2$ mentioned above, because doping a Mott insulator with one more electron per site causes the disappearance of its upper Hubbard band, whereas doping a band insulator leads to a rigid band

shift [172].

(iii) Ultrafast dynamics. Upon light pumping across the bandgap, Mott insulators and band insulators may "melt" at different time scales [182–185]. One complication is that in these materials the possible Mott insulating phase is built on top of a CDW lattice, which itself has a strong dynamical response by exciting CDW amplitude oscillations [182, 184], or by transforming into meta-stable "hidden" CDW phases [163, 186, 187].

(iv) Magnetic measurements. Naively, a Mott insulator hosts a lattice of spin-1/2 magnetic moments, while a non-magnetic band insulator does not. Magnetic measurements should therefore tell their difference. See section 3.3 for more details.

Readers interested in these directions, especially (i) and (ii), are referred to a recent dedicated review [188].

The advancement in the synthesis of 2D materials enables a different, perhaps more direct, strategy:

(v) Remove interlayer coupling (by studying a single layer), then add it back systematically (by adding to the material one layer at a time).

The idea is straightforward. One should first test whether the Mott and possibly QSL states can be established in the most probable scenario, that is a single layer where the interlayer effects are absent. After that, one can further interrogate if these exotic states can survive interlayer coupling and persist in bulk materials.

Single layers of $1T$-NbSe$_2$ [189], $1T$-TaS$_2$ [190], and $1T$-TaSe$_2$ [152, 191] have been grown using MBE. All three single-layer materials host $\sqrt{13} \times \sqrt{13}$ CDW, similar to their bulk counterparts (Fig. 4(a)). Inside a single-layer CDW lattice, each CDW unit cell should contain an odd number of 13 electrons (charge transfer from graphene substrate has been shown to be negligible for $1T$-TaSe$_2$ [152]). As a result, the band-insulator argument fails at the single-layer limit.

In the following, we use single-layer $1T$-TaSe$_2$ as a model system to introduce the electronic structure measurements, but we also comment on the material-specific differences when necessary.

As shown in Fig. 4, STM and ARPES spectra of single-layer $1T$-TaSe$_2$ exhibit a fully insulating electronic structure. From STS, the zero LDOS region bracketing the Fermi level (E_{F}) yields an energy gap of magnitude 109 ± 18 meV (Fig. 4(b)), and this gapped electronic structure is observed uniformly over the entire single-layer $1T$-TaSe$_2$ surface. ARPES spectra measured at 12 K confirm the insulating nature of single-layer $1T$-TaSe$_2$ (Fig. 4(c) and (d)). At low binding energies, the ARPES spectra show clear gapped intensity at all observed momenta, although the signal from coexisting $1H$-TaSe$_2$ islands can be seen crossing E_{F} [94] at $k \approx 0.5$ Å^{-1} (white dashed lines). The CDW superlattice potential induces band folding into a smaller CDW Brillouin zone (Fig. 4(d) inset). One such band can be seen in the ARPES spectrum for p-polarized light that shows a prominent flat band centered at $E - E_F \approx -0.26$ eV within the first CDW Brillouin zone (black dashed box). A more dispersive band can be resolved outside the

first CDW Brillouin zone boundary (vertical dashed lines labeled A and B mark this boundary). For *s*-polarized light (Fig. 4(d)), the flat band is much less visible, and a manifold of highly dispersive bands near the Γ-point dominates the spectrum. Similar insulating STS and ARPES spectra are also observed in single-layer $1T$-NbSe$_2$ [189,192] and $1T$-TaS$_2$ [193].

Two additional pieces of evidence support the observed single-layer insulating phase as a Mott insulator. First, DFT calculations show a half-filled flat band on the order of tens of meV in these single layers [149–152], hence prone to gap opening by Coulomb repulsion U. Indeed, Mott insulating band structures as predicted by DFT+U [152] show very similar features to the experimental observations. Second, as discussed in the next section, evidence of local moments in single-layer $1T$-TaSe$_2$ [194], $1T$-NbSe$_2$ [192], and $1T$-TaS$_2$ [195] have been observed through Kondo resonance when placing the $1T$
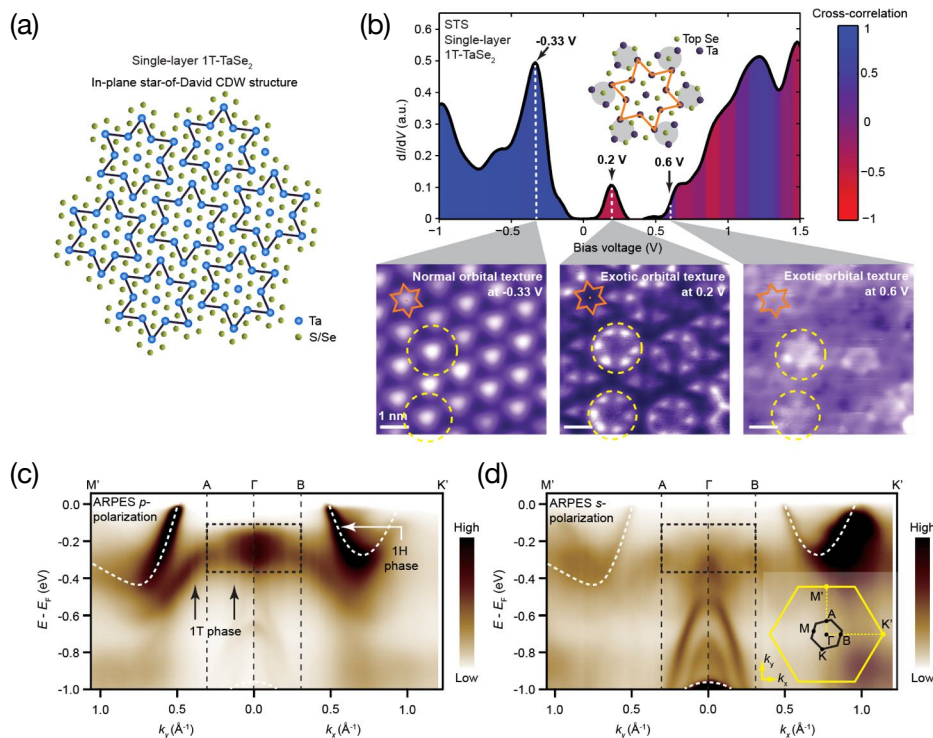

Figure 4. Mott insulating ground state in single-layer $1T$-TaSe$_2$. (a) Schematic of in-plane $\sqrt{13} \times \sqrt{13}$ CDW in the $1T$-TaSe$_2$ material family. (b) STM/STS characterization of the Mott insulating state in single-layer $1T$-TaSe$_2$ at $T = 5$ K. Insets show STM imaging of electronic states in lower Hubbard band (at $\sim$ -0.33 V), upper Hubbard band 1 (at $\sim$ 0.2 V), and upper Hubbard band 2 (at $\sim$ 0.6 V). The latter two are identified due to their unusual complimentary textures. (c and d) ARPES spectra of the Mott insulating state in single-layer $1T$-TaSe$_2$ at $T = 12$ K. A gapped electronic structure is seen except for electronic states from coexisting $1H$-TaSe$_2$ patches (white dashed lines). A flat band shows up in the first CDW Brillouin zone under *p*-polarized light (c) but not under *s*-polarized light (d), consistent with a d_{z^2} orbital composition of the flat band. All panels are modified from Ref. [152].

Mott layers onto corresponding $1H$ metallic layers.

One thing that theoretical calculations fail to show for single-layer $1T$-TaSe$_2$ [152] and single-layer $1T$-NbSe$_2$ [196, 197] is the exotic orbital texture observed at the upper Hubbard band (UHB) at a bias voltage of around 0.2 V (Fig. 4(b)). Here, instead of reproducing the lower Hubbard band (LHB) feature at -0.33 eV, the electronic LDOS form a "flower"-like pattern with low LDOS at the center of each CDW cell. Interestingly, such exotic orbital texture has not been observed in single-layer $1T$-TaS$_2$ [193]. Although a first-principles understanding has not been obtained, it was realized that the flower LDOS pattern at 0.2 V corresponds to the lowest-repulsion regions from a triangular lattice of occupied LHB electrons [152]. In contrast, the LDOS pattern at 0.6 V, with complimentary LDOS near centers of CDW cells, seems to correspond to higher-repulsion regions. Hence, it was interpreted that an original half-filled band is split into three Hubbard subbands (not two as in "ordinary" Mott insulator): an LHB at -0.33 V, a UHB$_1$ at 0.2 V, and a UHB$_2$ at 0.6 V. As side evidence, at elevated temperatures, the LDOS intensity at UHB$_2$ has been seen to jump back to UHB$_1$, hence forming a normal orbital texture similar to LHB. More investigation is required to provide a better understanding of this puzzle.

Having established that single-layer $1T$ materials are Mott insulators, one may ask the following questions: What role does the interlayer coupling play? How does a Mott-insulating $1T$-TaSe$_2$ single layer evolve into a bulk metal? As a first step towards answering this question, STS measurements of small MBE-grown bilayer and trilayer $1T$-TaSe$_2$ islands show increasingly weaker insulating behavior [152]. A recent more careful study [198] shows different results by using thin flakes of $1T$-TaSe$_2$ exfoliated from bulk crystals which are then investigated in a thickness-controlled manner. Transport measurements revealed a Mott-metal transition occurring above a thickness of 7 layers. Surface-sensitive STM spectroscopy measurements, however, revealed a Mott state from single-layer to bulk samples at the surface. To obtain a better understanding of this apparent contradiction, ARPES measurement was performed [198], which probes deeper into the bulk than STM. A metallic band crossing E_F was observed in samples thicker than 7 layers but was absent otherwise. Combined with DFT calculations, this observation provides evidence that interlayer coupling remarkably broadens the correlated band and turns $1T$-TaSe$_2$ from a Mott insulator in the single-layer form to a metal in the bulk form. At the same time, the surface of a crystal still exhibits Mott behavior due to reduced coordination and reduced coupling to bulk. In addition, unlike $1T$-TaS$_2$, which experiences layer dimerization that could lead to a band insulator [166, 199], $1T$-TaSe$_2$ does not show any signature of layer dimerization as evidenced by the ARPES data [198]. Therefore, Tian *et al.* [198] provide strong evidence that thin $1T$-TaSe$_2$ below 7 layers is a Mott insulator.
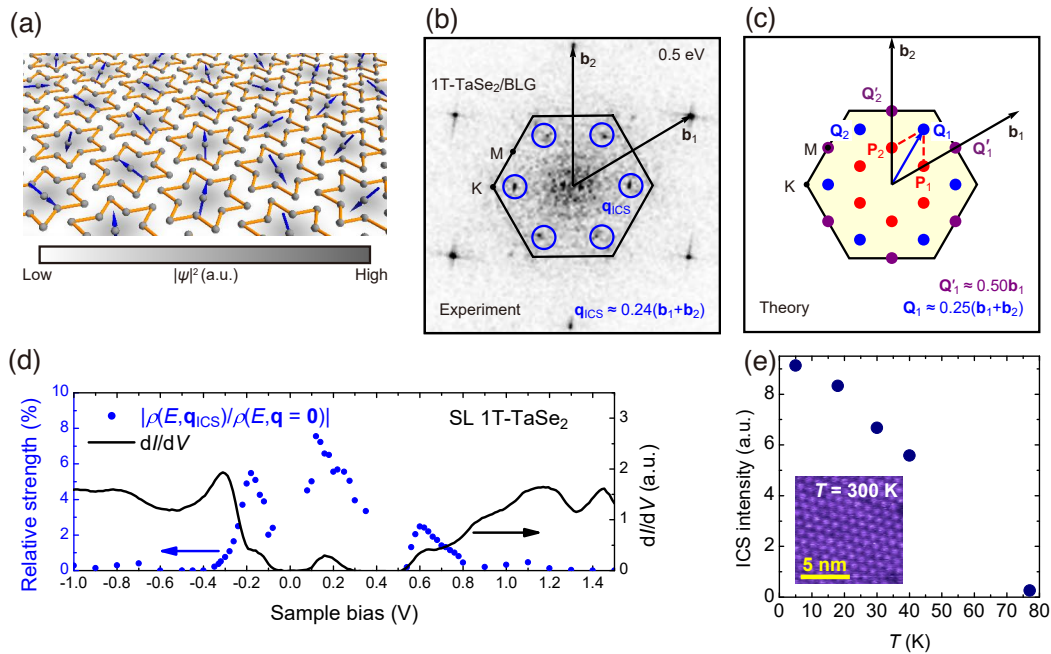
Figure 5. Imaging fractional spinons in a quantum spin liquid. (a) Schematic showing the star-of-David CDW lattice and localized magnetic moments centered at each star. (b) Fourier transform of an STM image scanned at 0.5 eV in single-layer $1T$-TaSe$_2$. (c) Theoretically predicted spinon spatial modulation vectors in a QSL. (d) Energy dependence of the observed super-modulation strength in single-layer $1T$-TaSe$_2$. (e) Temperature dependence of the observed super-modulation strength in single-layer $1T$-TaSe$_2$. The inset shows the star-of-David CDW modulation persisting to room temperature. All panels are reproduced from Ref. [194].

3.3. Signatures for quantum-spin-liquid state in single-layer $1T$-TaSe$_2$

Mott insulators with antiferromagnetically-coupled localized magnetic moments arranged in a frustrated lattice have long been regarded as ideal platforms where exotic quantum magnetic states such as QSL states might arise [200, 201]. QSLs refer to a class of magnetic ground states in which magnetic moments remain disordered due to frustration [202–206]. Above this exotic ground state, unusual, fractional excitations such as spinons are predicted to exist [202–206]. The recent investigation of the Mottness in $1T$-TaS$_2$ has brought new interest to possible QSL state in both $1T$-TaS$_2$ and $1T$-TaSe$_2$ [153], and it has been shown numerically that these materials might host a QSL with fermionic spinons forming a FS [154]. Experimental evidence for QSL in $1T$-TaS$_2$ has been collected [155–157, 207] but is under debate, possibly due to unwanted interlayer effects. In this regard, a single-layer 2D frustrated antiferromagnet is greatly desired to probe the intrinsic QSL behavior [153].

Two prerequisites for QSL are the existence of localized magnetic moments and the absence of magnetic ordering of these moments. Although a 2D spin lattice is ideal for testing intrinsic 2D QSL behavior, it poses great challenges in detection via

conventional magnetic probes. To test whether single-layer $1T$-TaSe$_2$ hosts a lattice of magnetic moments, a new electronic detection method based on the Kondo effect was utilized in a $1T/1H$-TaSe$_2$ heterobilayer [194, 208]. It was found that when single-layer $1T$-TaSe$_2$ is contacted to metallic single-layer $1H$-TaSe$_2$ in the $1T/1H$ heterobilayer, Kondo resonance develops in STM spectroscopy at most star-of-David sites. This verifies that each CDW supercell in single-layer $1T$-TaSe$_2$ indeed hosts a local magnetic moment [194], as indicated by the schematic in Fig. 5(a). Similar Kondo behavior has also been observed in single-layer $1T$-TaS$_2$ [195] and 1T-NbSe$_2$ [192, 197] when they are put into contact with the corresponding 1H layers.

Verification of the absence of long-range antiferromagnetic (AF) ordering down to the experimental base temperatures has been successfully carried out for bulk $1T$-TaS$_2$ [155–157, 207], but so far is still fulfilled for single-layer $1T$-TaSe$_2$. The best attempt up to date utilizes sensitive synchrotron-based x-ray magnetic dichroism [194], which shows magnetization less than 0.013 μ_B per star-of-David CDW cell at 2 K under 5 T magnetic field, indicating the absence of (ferro)magnetism in single-layer $1T$-TaSe$_2$ at least down to 2 K.

A direct, perhaps more desirable, method to test the QSL behavior is to verify the emergent fractional excitations. In most theoretical predictions for a triangular-lattice QSL, an electron would split into a chargeless spin-1/2 fermion (spinon) that forms a FS and a spinless charged boson (chargon) [200–206], a process known as the spin-charge separation. Although evidence of itinerant spinons has been obtained from thermal and magnetic measurements in many QSL candidates, key characteristics of the spinon FS are challenging to determine due to the fractional and chargeless nature of spinons. There have been theoretical proposals to probe the spinon FS properties based on unique characteristics of the spinons, such as Ruderman-Kittel-Kasuya-Yosida (RKKY) magnetism mediated by itinerant spinons [209], spinon Friedel oscillation that is detectable via conventional STM [210], and Kondo screening from itinerant spin-1/2 spinons [211]. In the following, we focus on two STM-based methods to provide evidence of spinons in single-layer $1T$-TaSe$_2$: (1) real-space imaging of the spinon wavefunction via conventional STM [194], and (2) STM spectroscopy of spinon-induced Kondo resonance resulting from the combined effect of spinon screening and emergent gauge fluctuations [212].

Conventional STM can be used to image fractional chargeless spinons because the tunneling probability depends on the real-space distribution of both spinons and chargons, thus providing a channel to reflect possible real-space oscillations of spinons due to their FS geometry [210] (while at the same time circumventing the difficulty in probing long-range magnetism in a single-layer material). When applying this technique to single-layer $1T$-TaSe$_2$ on a bilayer graphene substrate, no predicted Friedel oscillation was resolved, but a long-wavelength incommensurate super-modulation (ICS) at wavevector $\mathbf{q}_{ICS} \approx 0.249(\mathbf{b}_i + \mathbf{b}_{i+1})$ was instead observed [194] ($\mathbf{b}_i$ are the unit vectors of the CDW reciprocal lattice). Fig. 5(b) displays the Fourier transform image of a typical STM image acquired in the Hubbard band at 0.5 eV, which shows the $\mathbf{q}_{ICS}$ vector.
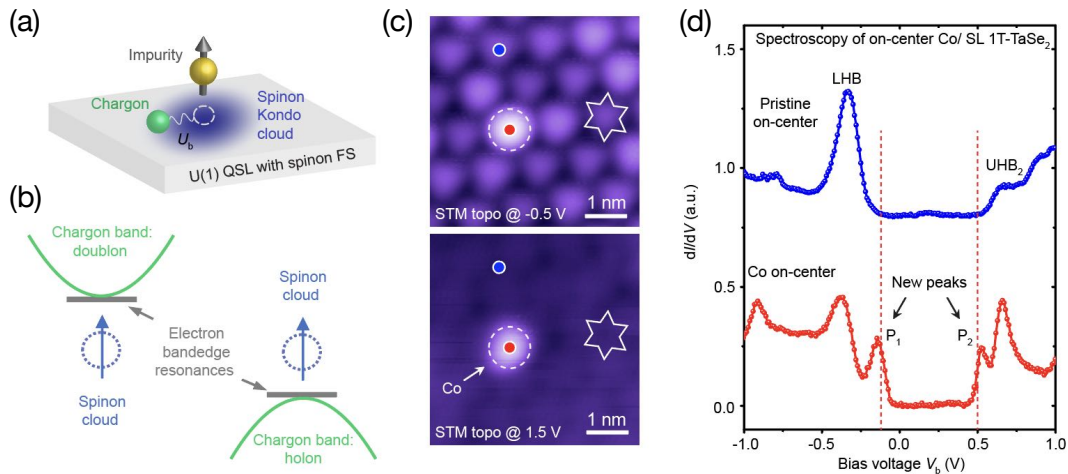
Figure 6. Probing a gapless quantum spin liquid with a magnetic impurity.
(a) Schematic showing spinon Kondo cloud formation around a magnetic impurity in a quantum spin liquid. Gauge binding interaction (U_b) additionally attracts a chargon to the spinon Kondo cloud, thereby forming a Kondo-induced resonance state. (b) Spectroscopically, such spinon-chargon resonance states should appear near the Hubbard band edges. (c) STM images of a single Co adatom on single-layer $1T$-TaSe$_2$ at negative and positive bias voltages. This Co adatom is located at a CDW supercell center, hence having the largest overlap with the charge distribution of $1T$-TaSe$_2$. (d) dI/dV spectra of pristine $1T$-TaSe$_2$ (blue curve) and a single Co adatom (red curve), both at the on-center position of a CDW cell (red/blue dots in (c)). Two new resonance peaks (labeled P_1 and P_2) appear near the Hubbard band edges for on-center Co. All panels are reproduced from Ref. [212].

If a QSL scenario with a spinon FS instability is adopted to explain the observed super-modulation, then one can find that q_{ICS} is right at the higher harmonic position (Q_i) of the predicted instability wavevectors $P_i \approx 0.249 b_i$ (i.e., $q_{ICS} = P_i + P_{i+1}$) as illustrated in Fig. 5(c). For another single-layer $1T$-TaSe$_2$ sample grown on a graphite substrate, an additional super-modulation wavevector $q_M \approx 0.5 b_i \approx 2 P_i$ was observed [194], which is also a higher harmonic of P_i. The fact that the observed super-modulation wavevectors coincide with higher harmonics of P_i can be explained by a composite spinon density wave order that forms out of primary spinon orders (e.g., pair density wave or spin density wave) at P_i [213, 214]. In addition, the super-modulation occurs only at Hubbard band energies but vanishes elsewhere (Fig. 5(d)), suggesting that it is a correlated phenomenon and consistent with the spin-charge separation picture. The different temperature-dependent behavior of the super-modulation and the star-of-David CDW (Fig. 5(e)) further rules out the possibility of the super-modulation being a conventional CDW induced by the star-of-David CDW. Therefore, the observation of the novel super-modulation via conventional STM provides important evidence for the QSL behavior in single-layer $1T$-TaSe$_2$.

A QSL with a spinon FS should act as a "neutral metal" and exhibit metallic behavior in the spin channel. A natural consequence is the spinon Kondo screening

around a magnetic impurity, providing another way to probe the itinerant spinons in a QSL (Fig. 6(a)). A single magnetic impurity in a U(1) QSL with a spinon FS has been investigated theoretically using a large-N expansion of a Kondo-like model coupled to a U(1) gauge field [211], and Kondo screening from itinerant spinons was found to appear despite the system being a charge insulator. Experimentally, the main evidence for spinon Kondo screening so far comes from muon spin rotation and relaxation studies conducted on a Kagome lattice QSL candidate, Zn-brochantite ($ZnCu_3(OH)_6SO_4$). Here the magnetic impurities, arising from Cu-Zn intersite disorder, were shown to exhibit reduced magnetic moments [215]. To provide more evidence for the spinon Kondo effect via spectroscopic characterization, magnetic Co atoms were deposited onto the surface of single-layer $1T$-TaSe$_2$ (Fig. 6(c)), and then STM spectroscopy was acquired on such magnetic adatoms [212]. Surprisingly, two resonance peaks arise right at the Hubbard band edges (Fig. 6(d)) when Co adatoms have maximal overlap with the charge distribution in a star-of-David supercell. It was also found that the resonance peaks disappear when Co adatoms are shifted away from the supercell center (both as-deposited adatoms and manually manipulated ones) [212]. They also vanish for nonmagnetic adatoms such as Au [212] and K. The above observations were explained as a combined effect of spinon Kondo screening and emergent gauge fluctuations (Fig. 6(b)): a spinon Kondo cloud forms around a magnetic impurity, serving as a strong attractive center for chargons that have the opposite emergent gauge charge from spinons. This attractive interaction thus yields two nearly symmetric composite spinonchargon states at energies both near the bottom of the doublon branch and near the top of the holon branch (Fig. 6(b)), in analogy to the donor and acceptor states of a semiconductor [212, 216].

Here two pieces of evidence for spinons in single-layer $1T$-TaSe$_2$ have been provided by STM measurement. We would also like to point out that the spinon interpretation, though best explaining the experimental observation at the current stage among other conventional explanations [194, 212], is speculative and needs further investigation. For instance, the strength of the emergent gauge field interaction needs to be carefully considered, which might lead to confined spinons and chargons [217], and thus failure of the spin-charge separation. The Friedel oscillations arising from spinon Fermi surface [210] are still absent in experimental observations.

4. Signatures of excitonic insulator in $1T$-ZrTe$_2$

The excitonic insulator is an intriguing condensed phase of matter where electron-hole pairs condense into a coherent macroscopic quantum state, analogous to BCS superconductivity [31, 32]. However, an unequivocal material realization of excitonic insulators has remained elusive despite intense theoretical and experimental efforts on several candidate materials [119–121, 218–224]. The materials family $1T$-TiSe$_2$, TiTe$_2$, and ZrTe$_2$ share an ideal electron band structure that is known to be advantageous to host an exciton condensate state [31, 32], with differences in the size of small band

gap or band overlap. The enhanced CDW transition temperature as the thickness goes down to ML [122, 124, 136] and the enlarged CDW gaps by varying dielectric substrate environments [130, 131] in $1T$-TiSe$_2$ and $1T$-TiTe$_2$ provide vital clues that enhanced excitonic interaction in atomically thin TMDCs [133–135]. The absence of CDW in bulk $1T$-ZrTe$_2$ indicates the suppressed inuence of electron-phonon interaction and a potential advantage in investigating excitonic instability.

Monolayer $1T$-ZrTe$_2$ has been grown by MBE on the graphitized SiC [225–228] and InAs(111) substrates [229]. At low temperatures, monolayer $1T$-ZrTe$_2$ enters a CDW-ordered state, evidenced by several clear experimental signatures [225, 226]. The ARPES measurements show the folding of the valence band and the opening of an energy gap between valence and conduction bands. The valence band top at the Γ point becomes flattened, and its spectral weight is almost entirely transferred to the folded valence band at the M point. Correspondingly, STM reveals a 2×2 superlattice pattern ($\mathbf{q}_{\mathrm{CDW}}$ = ($\frac{1}{2}$ $\frac{1}{2}$ 0)R0° r.l.u.) with contrast modulation reflecting the periodic lattice distortion
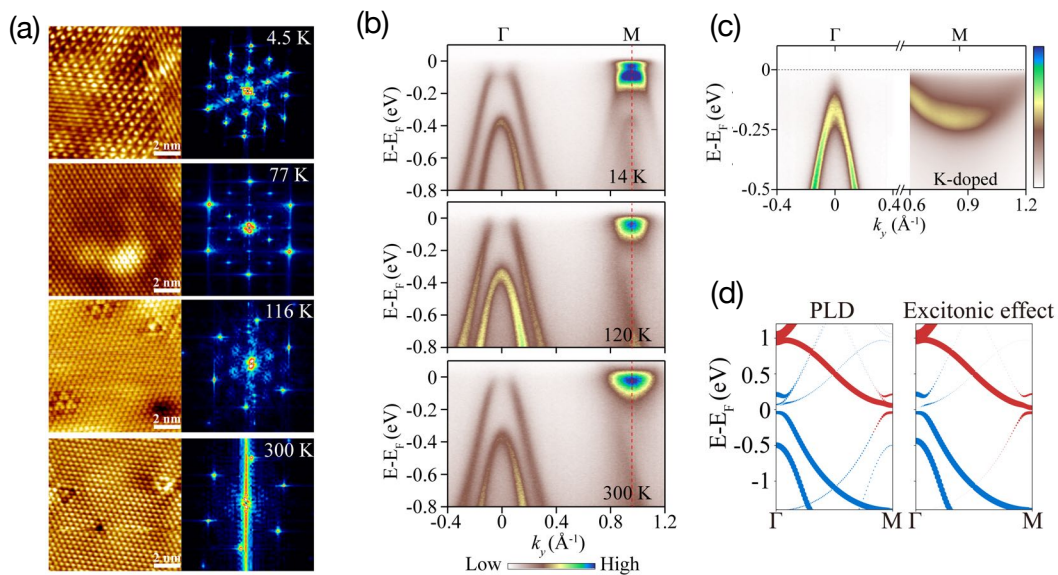

Figure 7. Excitonic condensation in monolayer $1T$-ZrTe$_2$ (a) Temperature dependent STM measurements on monolayer $1T$-ZrTe$_2$. The left panels of each temperature are topographic images, and the right panel is the Fourier transform of the image. The 2×2 superstructure peak is clearly visible at low temperatures, which diffuses and disappears at higher temperatures. (b) Temperature-dependent ARPES intensity maps of monolayer $1T$-ZrTe$_2$ clearly show the folding behavior at low temperatures (CDW phase). Even above the T_{CDW}, the intensity at the top of the valence band is depleted and a significant amount of spectral intensity still lies in the folded part of the spectrum. (c) Upon carrier doping, the system is driven into an interaction-suppressed normal state, exhibiting a two-step CDW transition. (d) The energy-dependent asynchronous band folding behavior is well-captured in theoretical calculations only with the inclusion of excitonic interactions. Figures are reproduced from Ref. [225].

(Fig. 7). As temperature increases, the CDW order is thermally suppressed. The gap size shrinks gradually and band folding intensity reduces. However, ARPES finds a significant amount of spectral weight is still transferred from the Γ point to the M point, as shown in Fig. 7(b) [225]. Concurrently, the superlattice contrast in STM becomes diffusive and finally disappears above the transition temperature T_{CDW}. The CDW phase of monolayer $1T$-ZrTe$_2$ is very sensitive to the sample thickness. Adding just one more layer causes significant deterioration of the CDW order [226].

The peculiarity of the CDW transition in monolayer $1T$-ZrTe$_2$ is that the system resides in an "intermediate" state at temperatures much higher than the CDW transition temperature, where only the top valence band at the Γ point shows folding and flattening and a significant amount of spectral weight is still transferred to the M-point to be the brightest part of the spectra [225] (Fig. 7). The second valence band at the higher energy around the Γ point follows the conventional CDW behavior, i.e., folding behavior completely disappears above T_{CDW}. This energy-dependent, asynchronous band folding behavior points to an unconventional mechanism different from a conventional electron-phonon interaction-driven CDW transition. Further evidence of non-conventional CDW transition comes from the carrier density dependence. By surface potassium doping or photo-charge injection, therefore moving away from the excitonic regime, Song *et al.* [225] revealed the $1T$-ZrTe$_2$ recovers a fully interaction-suppressed state, with sharp band dispersion and no gap (Fig. 7(c)), different from both CDW and non-CDW high-temperature state with energy-dependent partial band folding. Overall, the observations align well with theoretical signatures expected for an exciton gas phase at high temperatures (Fig. 7(d)) [225], which, upon condensation, induces the complete CDW order at low temperatures. The two-step transition with distinct band folding effects demonstrates the preformed excitonic nature of the instability in monolayer $1T$-ZrTe$_2$.

5. Novel CDW states in IrTe$_2$ and TaTe$_2$

The absence of interlayer coupling and subsequent changes in the electronic structure and symmetry in monolayer TMDCs is one of the promising ways to realize novel physical, chemical, and optical phenomena distinct from bulk. Previous sections indeed show some examples of such contrast, including the emergence of CDW transition in $1T$-TiTe$_2$ [122], the Mott insulating phase in ML $1T$-TaSe$_2$ [152], and excitonic condensation in ML $1T$-ZrTe$_2$ [225]. One of the less investigated ingredients in understanding the properties of ML TMDCs, or ML vdW materials in general, is how the varying interlayer coupling strength, which increases going from S, Se to Te, affects the changes of the material properties in ML limit [230]. In general, the stronger the interlayer coupling, the more dramatic changes are expected when it is completely deprived. However, the materials platform that shows such dramatic changes, close to the crossover from the vdW interaction to the covalent interaction, is rare due to the increased difficulty in both exfoliation and epitaxial growth as the interlayer interaction becomes stronger [231–233].

Among the family of TMDCs, $1T$-IrTe$_2$ is one of the unique materials since it has a shorter interlayer distance than the expected vdW bond length, indicating strong Te-Te interlayer coupling [234, 235]. The short bonding distance induces the formation of a polymeric $(Te_2)^{3-}$ and destabilizes the highly oxidized state of Ir, resulting in effective Ir^{3+} valence states [235, 236]. As a result, the formation of the polymeric Te-Te bond networks stabilizes the trigonal structure ($P\bar{3}m1$) with an Ir^{3+} valence state at high temperatures [235, 236]. Upon cooling, the polymeric Te-Te bonds are weakened, and the bulk $1T$-IrTe$_2$ undergoes a first-order-type transition to triclinic structure ($P1$) with Ir^{4+}-Ir^{4+} dimerization, exhibiting a sudden jump in resistivity [235].

Since the transition involves Ir $5d$ to Te $5p$ charge transfer with Te bond breaking, the system responds sensitively to interlayer coupling [234–236]. While Bulk $1T$-IrTe$_2$ shows two consecutive first-order transitions with superstructural modulation 5×1×5 at ∼ 280 K and 8×1×8 at 180 K [235], the surface shows multiple transitions as well as 6×1 structural phase [237, 238], which is not obtained in bulk. When the interlayer coupling is weakened by substituting Te with Se, not only the transition temperature is further enhanced up to 560 K, but also a distinct transformation of the superstructure from 5×1×5 to 6×1×6 occurs [239], suggesting the significant role of the Te-Te interlayer coupling in $1T$-IrTe$_2$. Considering the Te-Te interlayer coupling is much stronger compared to other TMDCs [234–236] and still exists in both surface and Se-substituted $1T$-IrTe$_2$ [239], ML $1T$-IrTe$_2$ is expected to show a dramatic change in structural and electronic properties due to the complete absence of the Te-Te interlayer coupling.

High-quality ML $1T$-IrTe$_2$ films were synthesized using MBE on BLG/SiC substrate [240]. Surprisingly, ML $1T$-IrTe$_2$ only exhibits a 2×1 Ir dimerized structure (a complete dimerization), which has never been obtained in bulk $1T$-IrTe$_2$ samples, without any transition up to 300 K [240]. As shown in Fig. 8, a more interesting finding is that the 2×1 dimer ground state shows a large-gap insulating state with a gap size larger than 1 eV, in contrast to the metallic 5×1 and 6×1 phases of BL as well as surface and Se-substituted $1T$-IrTe$_2$ [238, 239]. First-principles calculations reveal the existence of both charge and phonon instabilities at M point in ML $1T$-IrTe$_2$, suggesting that the 2×1 dimer structure in ML may be driven by the Peierls-type CDW transition with $\mathbf{q}_{CDW} = (\frac{1}{2}\ 1\ 0)$R0° r.l.u. [240]. However, the experimentally obtained results for ML $1T$-IrTe$_2$ strongly deviate from the Peierls-type CDW features. While typical CDW formation induces 1∼7% lattice contraction [4], ML $1T$-IrTe$_2$ shows 20% lattice contraction with a heavy electronic reconstruction and a huge energy band gap [240]. Since these features are too large to be explained by conventional CDW pictures [4], another essential ingredient, such as the local Ir bond formation [241, 242], should be added for a fuller explanation. Generally, partially filled Ir compounds prefer locally forming a direct Ir-Ir singlet because of their extended $5d$ orbital natures [241]. ML $1T$-IrTe$_2$ has an edge-sharing octahedral structure and only Ir^{4+} valence state with one hole owing to the total absence of the Te-Te interlayer coupling. Even though it is difficult to discern whether Peierls-like instability or local bond formation is more
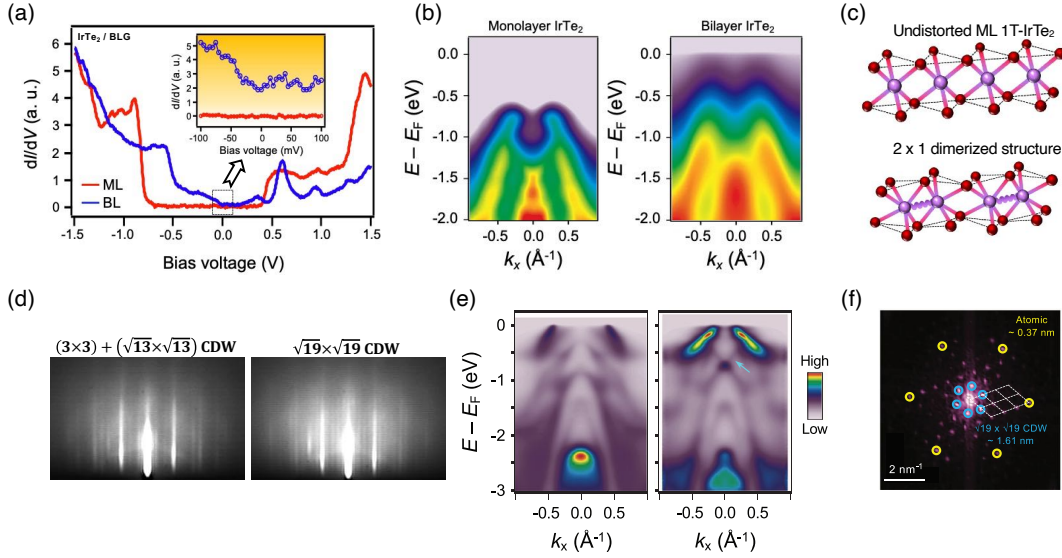
Figure 8. Novel CDW orders in IrTe$_2$ and TaTe$_2$ (a) The STS dI/dV spectra for ML and BL IrTe$_2$. The inset is a close-up of the black dashed box near Fermi energy (b) The ARPES intensity maps for ML and BL IrTe$_2$. (c) The crystal structures of the undistorted ML 1T-IrTe$_2$ and 2×1 dimerized one. (d) RHEED images from the different annealing conditions of 1T-TaTe$_2$. Left panel is after 340°C annealing, which leads to a mixture of 3×3 and $\sqrt{13} \times \sqrt{13}$ CDW. Right panel is after 400°C annealing that results in a $\sqrt{19} \times \sqrt{19}$ superstructure. (e) The ARPES spectra from different CDW orders, 3×3 and $\sqrt{13} \times \sqrt{13}$ (left) and $\sqrt{19} \times \sqrt{19}$ (right). (f) Fourier transform of STM image verifies the formation of $\sqrt{19} \times \sqrt{19}$ CDW. Figures are reproduced from Refs. [240, 243].

dominant or which one triggers the other in the dimer formation, once any perturbations are triggered, the effect of both mechanisms amplifies each other, making the heavy electronic reconstruction with the large band gap and massive lattice distortion as described in Fig. 8.

The large-gap insulating 2×1 dimer structure in ML completely disappears in BL 1T-IrTe$_2$ (Fig. 8). In the case of BL, the recovered Te-Te interlayer coupling suppresses the charge instability owing to the split of FS and eliminates the phonon softening. Moreover, the Ir^{3+} state partially exists in a BL-like surface state from the polymeric Te-Te interlayer coupling, which prevents the formation of the fully dimerized structure as in ML. The suppression of the CDW instability in BL does not allow the fully dimerized 2×1 structure. Instead, 6×1 and 5×1 phases are obtained as the ground states like surface and Se-Substituted 1T-IrTe$_2$ [238, 239]. This metal-to-insulator transition from BL to ML 1T-IrTe$_2$ indicates that the strong Te-Te interlayer coupling dramatically affects the phonon and charge instabilities in 1T-IrTe$_2$, thus playing a vital role in defining the charge-ordered ground states of 1T-IrTe$_2$.

1T-TaTe$_2$ is another good testbed to investigate the effect of stronger interlayer coupling on CDW states. As described in Section 3, 1T-TaS$_2$ and 1T-TaSe$_2$ form a $\sqrt{13} \times \sqrt{13}$ star-of-David CDW, which persists even down to ML limit. On the other

hand, $1T$-TaTe$_2$ exhibits 3×1×3 and 3×3×3 CDW orders with double zigzag chain and butterfly-like clusters due to the stronger Te-Te interlayer coupling and the significant charge transfer to Ta atoms, resulting in Jahn-Teller distortion [115,116,230]. Compared to $1T$-TaS$_2$ and $1T$-TaSe$_2$, which have the same crystal symmetry as $1T$-TaTe$_2$, natural questions arise what type of CDW order emerges when the strong Te-Te interlayer coupling gets completely removed in the ML form of $1T$-TaTe$_2$: Does ML still have 3×3 or 3×1 CDW orders like the bulk or transform to $\sqrt{13} \times \sqrt{13}$ CDW order with Mott insulating state as obtained in the sister compounds $1T$-TaS$_2$ and $1T$-TaSe$_2$? Or, would the electronic structure of ML $1T$-TaTe$_2$ be entirely modified by the absence of the Te-Te interlayer coupling and result in a distinct CDW order, as is the case of $1T$-IrTe$_2$?

These questions have been answered by investigating the ML $1T$-TaTe$_2$ films grown on BLG substrate using MBE [243, 244]. Surprisingly, ML $1T$-TaTe$_2$ exhibits a variety of metastable CDW orders, including 3×3, $\sqrt{13}\times\sqrt{13}$, and unprecedented $\sqrt{19}\times\sqrt{19}$ superstructures (Fig. 8). The multiple CDW orders in ML $1T$-TaTe$_2$ can be selectively stabilized by controlling the post-growth annealing temperature. Once a new CDW order is obtained by annealing at a higher temperature, it does not turn back to the previous CDW orders by annealing at the lower temperature. Moreover, the Mott-insulating state obtained in ML $1T$-TaSe$_2$ is not observed despite the formation of $\sqrt{13}\times\sqrt{13}$ CDW order in ML $1T$-TaTe$_2$ due to the less electronegativity and extended nature of Te atoms [115]. The most impressive feature in ML $1T$-TaTe$_2$ is that $\sqrt{19}\times\sqrt{19}$ CDW order is found with $\mathbf{q}_{\text{CDW}} = (\frac{1}{\sqrt{19}} \ \frac{1}{\sqrt{19}} \ 0)$R36.6° r.l.u., which has rarely been predicted nor reported in TMDCs. The experimental evidence of $\sqrt{19}\times\sqrt{19}$ CDW order in $1T$-TaTe$_2$ was confirmed by RHHED, STM, and ARPES measurements (Fig. 8), and it persists up to 8 layers for epitaxially-grown $1T$-TaTe$_2$ thin films [243]. DFT calculations supported the stability of the distinct $\sqrt{19}\times\sqrt{19}$ CDW order as well as 3×3 and $\sqrt{13}\times\sqrt{13}$ in ML $1T$-TaTe$_2$ by demonstrating stable phonon dispersion and the minimal difference of the relative total energy among three distinct CDW orders [243].

The epitaxially-grown ML $1T$-NbTe$_2$ also displays multiple CDW orders, including 4×1, 4×4, $\sqrt{19}\times\sqrt{19}$, and even larger $\sqrt{28}\times\sqrt{28}$ superstructures with $\mathbf{q}_{\text{CDW}} = (\frac{1}{\sqrt{28}} \ \frac{1}{\sqrt{28}} \ 0)$R7° r.l.u. [245] controlled by the post-annealing temperature with an irreversible process, in a similar way as ML $1T$-TaTe$_2$. The origin of the unexpected $\sqrt{19}\times\sqrt{19}$ and $\sqrt{28}\times\sqrt{28}$ CDW orders is not fully understood yet because the conventional pictures of CDW transition, such as Peierls instability or momentum-dependent strong electron-phonon coupling, are not clearly connected in these systems [243, 245]. Nonetheless, the emergence of new types of CDW orders in the ML TMDCs strongly indicates that the stronger interlayer coupling in the Te system plays a significant role in creating a dramatic transformation of quantum orders.

6. Summary and Outlook

In summary, we have reviewed various CDW orders and accompanying quantum phenomena on epitaxially grown 2D TMDCs. We have mainly focused on the electronic

structures investigation using ARPES and STM/STS as complementary experimental probes.

We have found that the changes in the CDW order at the atomically thin 2D limit from that of bulk are heavily material-dependent despite the commonly imposed conditions of deprived interlayer coupling, broken symmetry, and consequent changes in electronic structure. In some cases, such as $1H$-NbSe$_2$, $1H$-TaSe$_2$, and $1T$-TaSe$_2$, the CDW ordering vector in the monolayer limit is exactly the same as that of bulk. The T_{CDW} exhibits only moderate changes, while coexisting SC gets suppressed dramatically. In other cases, monolayer $\mathbf{q}_{\mathrm{CDW}}$ becomes vastly different from that of bulk. Examples include $1T$-VSe$_2$, $1T$-VTe$_2$, $1T$-TiSe$_2$, and $1T$-IrTe$_2$. There has also been the case that CDW order emerges only in the monolayer limit, while it is absent in the bulk, as witnessed in $1T$-TiTe$_2$ and $1T$-ZrTe$_2$. These various examples show us that the material-specific details, e.g., strength and character of interlayer bonding, orbital characters of transition metal atoms, charge carrier density, and Fermi energy filling, all play essential roles in building up this prototypical cooperative electronic phase.

We have also reviewed how exotic electronic orders emerge in connection with the 2D CDW in monolayer TMDCs. A prime example is the Mott insulating state with unusual orbital texture in monolayer $1T$-TaSe$_2$. We have further discussed the evidence of the QSL state from STM, which includes the supermodulation in Fourier-transformed STM data corresponding to the spinon FS and the spinon Kondo effect when a magnetic impurity is added at the charge modulation center. The excitonic insulator has been studied extensively in recent years, and the CDW state in $1T$-ZrTe$_2$ was discussed in that context. The asynchronous band folding and spectral weight transfer, along with the two-step CDW transition, provide strong spectroscopic evidence that monolayer $1T$-ZrTe$_2$ may indeed be an excitonic condensate.

New types of charge order and CDWs are found in the monolayer of IrTe$_2$, in which a Peierls-like FS instability and local bond formation cooperatively enhance and stabilize the fully dimerized charge order state. Finally, large cell superstructures such as $\sqrt{19} \times \sqrt{19}$ and $\sqrt{28} \times \sqrt{28}$, rarely reported previously, have been found in $1T$-TaTe$_2$ and $1T$-NbTe$_2$ through controlled post-growth annealing.

In this review, we have limited ourselves to the 2D CDW orders and surrounding phenomena that are realized in a single materials platform for a focused discussion. However, there are many classical materials systems that have been investigated in the context of CDW order and competing electronic phases. Well-known examples include rare earth tritellurides [246], molybdenum bronzes [247], and even cuprates [248, 249]. It would be of tremendous interest to realize the 2D form of these materials and study how the CDW itself evolves in the atomically thin 2D limit, how the potential changes in the CDW impact other coexisting orders, and whether there are any novel physical properties associated with it [250, 251]. α-phase uranium (α-U) takes a special place as being the only single element material that exhibits a series of low-temperature CDW transitions [252]. It also makes a transition into an SC as the temperature further decreases. Thin films of α-U have been grown on substrates such as Nb

and W, and show a great enhancement of T_{CDW} due to the epitaxial strain from the substrates, suggesting a possibility of controlling CDW order using strain [253]. Further investigation on atomically thin α-U and the potential interplay between CDW and SC would be immensely interesting. Another fascinating recent development not discussed in the review is the CDW phases in Kagome materials, in which the CDW coexists with other emerging orders, such as orbital order, electronic nematicity, SC, and topological orders [16–18]. The epitaxial growth of Kagome thin films is still in its early stage [254, 255]. Whether the epitaxial thin film down to a few layers of thickness can be achieved with high enough quality to be measured by ARPES and STM remains to be seen.

By stacking 2D materials into lateral and vertical heterostructures with varying relative orientations, one can achieve novel physical, chemical, and optical properties that are not easily attainable in constituent materials themselves [256, 257]. The CDW phenomena at the domain boundaries of 2D TMDCs have been previously studied [69, 70]. Whether a similar CDW would arise at the boundaries of lateral heterostructures of other 2D materials is currently unclear. The realization of correlated electronic phases in twisted bilayer graphene ignited an intense research effort on twisted vertical heterostructures of 2D materials [257]. Experimental and theoretical efforts are underway to find out how the complex order parameters with potentially different symmetries would affect each other when assembled into a heterostructure with well-defined relative orientation. Materials with 2D CDW would provide an essential member of the materials library for such research effort.

Many 2D TMDCs presented in this review are waiting to be measured with other experimental probes (some of which were introduced in Section 1) that have been crucial in revealing the CDW orders in bulk materials. While some of the scattering-based measurements are challenging for the few-layer samples due to the lack of scattering centers in the 2D layers, other techniques are mainly limited by the availability of samples and difficulty in sample transfers among ultra-high vacuum systems. A tight integration of sample growth and characterization tools, as well as continued improvements in the photon, electron, neutron sources, and detection technology, may close this gap. It would be fascinating to apply, e.g., time-resolved ARPES [119] and x-ray scattering [13, 14] measurements on the CDW phases discussed in this review to gain further insight into their origins and coexisting orders.

To conclude, we believe there remains much to be explored in the complex electronic phases of atomically thin 2D materials. As the materials library expands with advanced synthesis, *in situ* sample manipulation, and heterostructure stacking, and as the experimental tools improve with better precision and stability, a more profound understanding of complex quantum phases will become possible and contribute to the development of future electronic, spintronic and quantum devices.

Acknowledgments

Data Availability

The data that support the findings of this study are available upon request from the authors.

References

[1] Grüner G 1994 *Density Waves in Solids* (Perseus Publishing, Cambridge, MA)
[2] Grüner G 1988 The dynamics of charge-density waves *Rev. Mod. Phys.* **60** 112982
[3] Friend R H and Jerome D 1979 Periodic lattice distortions and charge density waves in one- and two-dimensional metals *J. Phys. C: Solid State Phys.* **12** 144177
[4] Rossnagel K 2011 On the origin of charge-density waves in select layered transition-metal dichalcogenides *J. Phys. Condens. Matter.* **23** 213001
[5] Chen C-W, Choe J and Morosan E 2016 Charge density waves in strongly correlated electron systems *Rep. Prog. Phys.* **79** 084505
[6] Zhu X, Guo J, Zhang J and Plummer E W 2017 Misconceptions associated with the origin of charge density waves *Advances in Physics: X* **2** 62240
[7] Fröhlich H 1954 On the theory of superconductivity: the one-dimensional case *Proc. R. Soc. Lond. Ser. A Math. Phys. Sci.* **223** 296305
[8] Peierls R E 1955 *Quantum Theory of Solids* (Oxford University Press, New York)
[9] Fogle W and Perlstein J H 1971 Semiconductor-to-metal transition in the blue potassium molybdenum bronze, $K_{0.30}MoO_3$; Example of a possible excitonic insulator *Phys. Rev. B* **6** 140212
[10] Moneau P, Ong N P, Portis A M, Meerschaut A and Rouxel J 1976 Electric field breakdown of charge-density-waveinduced anomalies in $NbSe_3$ *Phys. Rev. Lett.* **37** 6026
[11] Zhu X, Cao Y, Zhang J, Plummer E W and Guo J 2015 Classification of charge density waves based on their nature *Proc. Natl. Acad. Sci.* **112** 236771
[12] Gabovich A M, Voitenko A I, Annett J F and Ausloos M 2001 Charge- and spin-density-wave superconductors *Supercond. Sci. Technol.* **14** R1

[13] Lee W-S 2021 X-ray studies of the CDW ground state and excitations in high-T_C cuprates *J. Phys. Soc. Jpn.* **90** 111004

[14] Arpaia R and Ghiringhelli G 2021 Charge order at high temperature in cuprate superconductors *J. Phys. Soc. Jpn.* **90** 111005

[15] Xu Z, Yang H, Song X, Chen Y, Yang H, Liu M, Huang Z, Zhang Q, Sun J, Liu L and Wang Y 2021 Recent progress of charge density waves in 2D transition metal dichalcogenide-based heterojunctions and their applications *Nanotechnology* **32** 492001

[16] Nie L *et al.* 2022 Charge-density-wave-driven electronic nematicity in a kagome superconductor *Nature* **604** 5964

[17] Kang M *et al.* 2023 Charge order landscape and competition with superconductivity in kagome metals *Nat Mater* **22** 18693

[18] Teng X *et al.* 2023 Magnetism and charge density wave order in kagome FeGe *Nat. Phys.* **19** 81422

[19] Wilson J A, Salvo F J D and Mahajan S 1975 Charge-density waves and superlattices in the metallic layered transition metal dichalcogenides *Adv. Phys.* **24** 117201

[20] Yang H, Kim S W, Chhowalla M and Lee Y H 2017 Structural and quantum-state phase transition in van der Waals layered materials *Nat. Phys.* **13** 9317

[21] Geim A K and Grigorieva I V 2013 Van der Waals heterostructures *Nature* **499** 41925

[22] Burch K S, Mandrus D and Park J-G 2018 Magnetism in two-dimensional van der Waals materials *Nature* **563** 4752

[23] Splendiani A, Sun L, Zhang Y, Li T, Kim J, Chim C-Y, Galli G and Wang F 2010 Emerging photoluminescence in monolayer MoS_2 *Nano Lett.* **10** 12715

[24] Mak K F, Lee C, Hone J, Shan J and Heinz T F 2010 Atomically thin MoS_2: A new direct-gap semiconductor *Phys. Rev. Lett.* **105** 136805

[25] Gweon G H, Denlinger J D, Clack J A, Allen J W, Olson C G, DiMasi E, Aronson M C, Foran B and Lee S 1998 Direct observation of complete Fermi surface, imperfect nesting, and gap anisotropy in the high-temperature incommensurate charge-density-wave compound $SmTe_3$ *Phys. Rev. Lett.* **81** 8869

[26] Gweon G H, Allen J W, Clack J A, Zhang Y X, Poirier D M, Benning P J, Olson C G, Marcus J and Schlenker C 1997 Direct Fermi-surface image of hidden nesting for $NaMo_6O_{17}$ and KMo_6O_{17} *Phys. Rev. B* **55** 133536

[27] Johannes M D and Mazin I I 2008 Fermi surface nesting and the origin of charge density waves in metals *Phys. Rev. B* **77** 165135

[28] Johannes M D, Mazin I I and Howells C A 2006 Fermi-surface nesting and the origin of the charge-density wave in $NbSe_2$ *Phys. Rev. B* **73** 205102

[29] Weber F, Rosenkranz S, Castellan J P, Osborn R, Hott R, Heid R, Bohnen K P, Egami T, Said A H and Reznik D 2011 Extended phonon collapse and the origin of the charge-density wave in 2H-$NbSe_2$ *Phys. Rev. Lett.* **107** 107403

[30] Rice T M and Scott G K 1975 New mechanism for a charge-density-wave instability *Phys. Rev. Lett.* 35 1203

[31] Kohn W 1967 Excitonic phases *Phys. Rev. Lett.* **19** 43942

[32] Jerome D, Rice T M and Kohn W 1967 Excitonic insulator *Phys. Rev.* **158** 46275

[33] Moulding O, Muramatsu T, Sayers C J, Como E D and Friedemann S 2022 Suppression of charge-density-wave order in $TiSe_2$ studied with high-pressure magnetoresistance *Electron. Struct.* **4** 035001

[34] Demsar J, Forr L, Berger H and Mihailovic D 2002 Femtosecond snapshots of gap-forming charge-density-wave correlations in quasi-two-dimensional dichalcogenides 1T-TaS_2 and 2H-$TaSe_2$ *Phys. Rev. B* **66** 041101

[35] Zhou X, Li Y, Fan X, Hao J, Dai Y, Wang Z, Yao Y and Wen H-H 2021 Origin of charge density wave in the kagome metal CsV_3Sb_5 as revealed by optical spectroscopy *Phys. Rev. B* **104** L041101

[36] Psztor , Scarfato A, Spera M, Flicker F, Barreteau C, Giannini E, Wezel J van and Renner C 2021 Multiband charge density wave exposed in a transition metal dichalcogenide *Nat. Commun.* **12**

6037

[37] Voit J, Perfetti L, Zwick F, Berger H, Margaritondo G, Grner G, Hchst H and Grioni M 2000 Electronic structure of solids with competing periodic potentials *Science* **290** 5013

[38] Ortiz B R, Teicher S M L, Kautzsch L, Sarte P M, Ratcliff N, Harter J, Ruff J P C, Seshadri R and Wilson S D 2021 Fermi surface mapping and the nature of charge-density-wave order in the kagome superconductor CsV_3Sb_5 *Phys. Rev. X* **11** 041030

[39] Brouet V, Yang W L, Zhou X J, Hussain Z, Ru N, Shin K Y, Fisher I R and Shen Z X 2004 Fermi surface reconstruction in the CDW State of $CeTe_3$ observed by photoemission *Phys. Rev. Lett.* **93** 126405

[40] Brouet V *et al.* Angle-resolved photoemission study of the evolution of band structure and charge density wave properties in RTe_3 (R=Y, La, Ce, Sm, Gd, Tb, and Dy) *Phys. Rev. B* **77** 235104

[41] Blackburn E *et al.* 2013 X-Ray diffraction observations of a charge-density-wave order in superconducting ortho-II $YBa_2Cu_3O_{6.54}$ single crystals in zero magnetic field *Phys. Rev. Lett.* **110** 137004

[42] Joe Y I *et al.* 2014 Emergence of charge density wave domain walls above the superconducting dome in $1T$-$TiSe_2$ *Nat. Phys.* **10** 4215

[43] Tsen A W *et al.* 2015 Structure and control of charge density waves in two-dimensional $1T$-TaS_2 *Proc. Natl. Acad. Sci.* **112** 150549

[44] Arguello C J *et al.* 2014 Visualizing the charge density wave transition in $2H$-$NbSe_2$ in real space *Physs Rev. B* **89** 235115

[45] Tomic A, Rak Z, Veazey J P, Malliakas C D, Mahanti S D, Kanatzidis M G and Tessmer S H 2009 Scanning tunneling microscopy study of the $CeTe_3$ charge density wave *Phys. Rev. B* **79** 085422

[46] Vinograd I, Zhou R, Mayaffre H, Krmer S, Liang R, Hardy W N, Bonn D A and Julien M-H 2019 Nuclear magnetic resonance study of charge density waves under hydrostatic pressure in YBa2Cu3Oy *Phys. Rev. B* **100** 094502

[47] Lin D *et al.* 2020 Patterns and driving forces of dimensionality-dependent charge density waves in $2H$-type transition metal dichalcogenides *Nat. Commun.* **11** 2406

[48] Cea T and Benfatto L 2014 Nature and Raman signatures of the Higgs amplitude mode in the coexisting superconducting and charge-density-wave state *Phys. Rev. B* **90** 224515

[49] Pouget J P, Hennion B, Escribe-Filippini C and Sato M 1991 Neutron-scattering investigations of the Kohn anomaly and of the phase and amplitude charge-density-wave excitations of the blue bronze $K_{0.3}MoO_3$ *Phys. Rev. B* **43** 842130

[50] Nguyen T *et al.* 2020 Topological singularity induced chiral Kohn anomaly in a Weyl semimetal *Phys. Rev. Lett.* **124** 236401

[51] Kwok R S, Gruner G and Brown S E 1990 Fluctuations and thermodynamics of the charge-density-wave phase transition *Phys. Rev. Lett.* **65** 3658

[52] Sobota J A, He Y and Shen Z-X 2021 Angle-resolved photoemission studies of quantum materials *Rev. Mod. Phys.* **93** 025006

[53] Mo S-K 2017 Angle-resolved photoemission spectroscopy for the study of two-dimensional materials *Nano Converg.* **4** 6

[54] Yang H, Liang A, Chen C, Zhang C, Schroeter N B M and Chen Y 2018 Visualizing electronic structures of quantum materials by angle-resolved photoemission spectroscopy *Nat. Rev. Mater.* **3** 341-53

[55] Moore R G, Brouet V, He R, Lu D H, Ru N, Chu J-H, Fisher I R and Shen Z-X 2010 Fermi surface evolution across multiple charge density wave transitions in $ErTe_3$ *Phys. Rev. B* **81** 073102

[56] Gweon G H, Mo S-K, Allen J W, Ast C R, Hchst H H, Sarrao J L and Fisk Z 2005 Hidden one-dimensional electronic structure and non-Fermi-liquid angle-resolved photoemission line shapes of η-Mo_4O_{11} *Phys. Rev. B* **72** 079903

[57] Rahn D J, Hellmann S, Kallne M, Sohrt C, Kim T K, Kipp L and Rossnagel K 2012 Gaps and kinks in the electronic structure of the superconductor $2H$-$NbSe_2$ from angle-resolved photoemission at 1 K *Phys. Rev. B* **85** 224532

[58] Jiang Z *et al.* 2023 Observation of electronic nematicity driven by the three-dimensional charge density wave in Kagome lattice KV_3Sb_5 *Nano Lett.* **23** 562533

[59] Gweon G H, Allen J W and Denlinger J D 2003 Generalized spectral signatures of electron fractionalization in quasi-one- and two-dimensional molybdenum bronzes and superconducting cuprates *Phys. Rev. B* **68** 195117

[60] Yang H F *et al.* 2022 Visualization of chiral electronic structure and anomalous optical response in a material with chiral charge density waves *Phys. Rev. Lett.* **129** 156401

[61] Monney C *et al.* 2010 Probing the exciton condensate phase in $1T$-$TiSe_2$ with photoemission *New J. Phys.* **12** 125019

[62] Bian K, Gerber C, Heinrich A J, Mller D J, Scheuring S and Jiang Y 2021 Scanning probe microscopy *Nat. Rev. Methods Prim.* **1** 36

[63] Meyer E, Bennewitz R and Hug H J 2021 *Scanning probe microscopy* (Springer Cham)

[64] Carpinelli J M, Weitering H H, Plummer E W and Stumpf R 1996 Direct observation of a surface charge density wave *Nature* **381** 398400

[65] Efferen C van *et al.* 2021 A full gap above the Fermi level: the charge density wave of monolayer VS_2 *Nat. Commun.* **12** 6837

[66] Sanna A, Pellegrini C, Liebhaber E, Rossnagel K, Franke K J and Gross E K U 2022 Real-space anisotropy of the superconducting gap in the charge-density wave material $2H$-$NbSe_2$ *npj Quantum Mater.* **7** 6

[67] Kim T-H and Yeom H W 2012 Topological solitons versus nonsolitonic phase defects in a quasi-one-dimensional charge-density wave *Phys. Rev. Lett.* **109** 246802

[68] Yeom H W, Oh D M, Wippermann S and Schmidt W G 2016 Impurity-mediated early condensation of a charge density wave in an atomic wire array *ACS Nano* **10** 8104

[69] Barja S *et al.* 2016 Charge density wave order in 1D mirror twin boundaries of single-layer $MoSe_2$ *Nat. Phys.* **12** 7516

[70] Zhu T *et al.* 2022 Imaging gate-tunable TomonagaLuttinger liquids in $1H$-$MoSe_2$ mirror twin boundaries *Nat. Mater.* **21** 74853

[71] Jones R O 2015 Density functional theory: Its origins, rise to prominence, and future *Rev. Mod. Phys.* **87** 897923

[72] Becke A D 2014 Perspective: Fifty years of density-functional theory in chemical physics *J. Chem. Phys.* **140** 18A301

[73] Hasnip P J, Refson K, Probert M I J, Yates J R, Clark S J and Pickard C J 2014 Density functional theory in the solid state *Philos. Trans. R. Soc. A: Math., Phys. Eng. Sci.* **372** 20130270

[74] Chowdhury S, Rigosi A F, Hill H M, Vora P, Walker A R H and Tavazza F 2022 Computational methods for charge density waves in 2D materials *Nanomaterials* **12** 504

[75] Himmetoglu B, Floris A, Gironcoli S and Cococcioni M 2014 Hubbardcorrected DFT energy functionals: The LDA+U description of correlated systems *Int. J. Quantum Chem.* **114** 1449

[76] Kim R and Son Y-W 2024 Transferable empirical pseudopotentials from machine learning *Phys. Rev. B* **109** 045153

[77] Moncton D E *et al.* 1977 Neutron scattering study of the charge-density wave transitions in $2H$-$TaSe_2$ and $2H$-$NbSe_2$ *Phys. Rev. B* **16** 801-819

[78] Borisenko S V *et al.* 2009 Two energy gaps and Fermi-surface arcs in $NbSe_2$ *Phys. Rev. Lett.* **102** 166402

[79] Chatterjee U *et al.* 2015 Emergence of coherence in the charge-density wave state of $2H$-$NbSe_2$ *Nat. Commun.* **6** 6313

[80] Flicker F and Wezel J van 2015 Charge order from orbital-dependent coupling evidenced by $NbSe_2$ *Nat. Commun.* **6** 7034

[81] Calandra M, Mazin I I and Mauri F 2009 Effect of dimensionality on the charge-density wave in few-layer $NbSe_2$ *Phys. Rev. B* **80** 241108

[82] Ugeda M M *et al.* 2016 Characterization of collective ground states in single-layer $NbSe_2$ *Nat. Phys.* **12** 927

[83] Giambattista B, Johnson A, Coleman R V, Drake B and Hansma P K 1988 Charge-density waves observed at 4.2 K by scanning-tunneling microscopy *Phys. Rev. B* **37** 27414

[84] Straub Th, Finteis Th, Claessen R, Steiner P, Hfner S, Blaha P, Oglesby C S and Bucher E 1999 Charge-density-wave mechanism in 2H-NbSe$_2$: photoemission results *Phys. Rev. Lett.* **82** 45047

[85] Onishi S *et al.* 2016 Selenium capped monolayer NbSe$_2$ for twodimensional superconductivity studies *Phys. Status Solidi B* **253** 23962399

[86] Xi X, Zhao L, Wang Z, Berger H, Forr L, Shan J and Mak K F 2015 Strongly enhanced charge-density-wave order in monolayer NbSe$_2$ *Nat. Nanotechnol.* **10** 7659

[87] Cao Y *et al.* 2015 Quality heterostructures from two-dimensional crystals unstable in air by their assembly in inert atmosphere *Nano Lett.* **15** 491421

[88] Rubio-Verd C *et al.* 2020 Visualization of multifractal superconductivity in a two-dimensional transition metal dichalcogenide in the weak-disorder regime *Nano Lett.* **20** 51118

[89] Xi X, Wang Z, Zhao W, Park J-H, Law K T, Berger H, Forr L, Shan J and Mak K F 2016 Ising pairing in superconducting NbSe$_2$ atomic layers *Nat. Phys.* **12** 13943

[90] Xu C-Z, Wang X, Chen P, Fltotto D, Hlevyack J A, Lin M-K, Bian G, Mo S-K and Chiang T-C 2018 Experimental and theoretical electronic structure and symmetry effects in ultrathin NbSe$_2$ films *Phys. Rev. Mater.* **2** 064002

[91] Xie X *et al.* 2021 Charge Density Wave and Electron-Phonon Interaction in Epitaxial Monolayer NbSe$_2$ Films *Chin. Phys. Lett.* **38** 107101

[92] Dreher P *et al.* 2021 Proximity effects on the charge density wave order and superconductivity in single-layer NbSe$_2$ *ACS Nano* **15** 194308

[93] Kumakura T, Tan H, Handa T, Morishita M, and Fukuyama H 1996 Charge density waves and superconductivity in 2H-TaSe$_2$ *Czech. J. Phys.* **46** 2611-2612

[94] Ryu H *et al.* 2018 Persistent charge-density-wave order in single-layer TaSe$_2$ *Nano Lett.* **18** 68994

[95] Moncton D E, Axe J D and DiSalvo F J 1975 Study of superlattice formation in 2H-NbSe$_2$ and 2H-TaSe$_2$ by neutron scattering *Phys. Rev. Lett.* **34** 7347

[96] Scholz G A *et al.* 1982 Charge density wave commensurability in 2H-TaS$_2$ and Ag$_x$TaS$_2$ *Solid State Communications* **44** 1455-1459

[97] Tsutsumi K 1982 X-ray-diffraction study of the periodic lattice distortion associated with a charge-density wave in 1T-VSe$_2$ *Phys. Rev. B* **26** 5756-5759

[98] Eaglesham D J, Withers R L and Bird D M 2000 Charge-density-wave transitions in 1T-VSe$_2$ *J. Phys. C: Solid State Phys.* **19** 359

[99] Jolie W, Knispel T, Ehlen N, Nikonov K, Busse C, Grneis A and Michely T 2019 Charge density wave phase of VSe$_2$ revisited *Phys. Rev. B* **99** 115417

[100] Strocov V N, Shi M, Kobayashi M, Monney C, Wang X, Krempasky J, Schmitt T, Patthey L, Berger H and Blaha P 2012 Three-dimensional electron realm in VSe$_2$ by soft-x-ray photoelectron spectroscopy: origin of charge-density waves *Phys. Rev. Lett.* **109** 086401

[101] Chen P, Pai W W, Chan Y H, Madhavan V, Chou M Y, Mo S-K, Fedorov A V and Chiang T-C 2018 Unique Gap Structure and Symmetry of the Charge Density Wave in Single-Layer VSe$_2$ *Phys. Rev. Lett.* **121** 196402

[102] Yilmaz T, Vescovo E and Sinkovic B 2023 Multiband Fermi surface in 1T-VSe$_2$ and its implication for the charge density wave phase *Phys. Rev. B* **107** 165109

[103] Terashima K, Sato T, Komatsu H, Takahashi T, Maeda N and Hayashi K 2003 Charge-density wave transition of 1T-VSe$_2$ studied by angle-resolved photoemission spectroscopy *Phys. Rev. B* **68** 155108

[104] Diego J, Said A H, Mahatha S K, Bianco R, Monacelli L, Calandra M, Mauri F, Rossnagel K, Errea I and Blanco-Canosa S 2021 van der Waals driven anharmonic melting of the 3D charge density wave in VSe$_2$ *Nat. Commun.* **12** 598

[105] Pandey J and Soni A 2020 Electron-phonon interactions and two-phonon modes associated with charge density wave in single crystalline 1T-VSe$_2$ *Phys. Rev. Res.* **2** 033118

[106] Duvjir G *et al.* 2018 Emergence of a metalinsulator transition and high-temperature charge-

density waves in VSe$_2$ at the monolayer limit *Nano Lett.* **18** 54328

[107] Feng J *et al.* 2018 Electronic structure and enhanced charge-density wave order of monolayer VSe$_2$ *Nano Lett.* **18** 44939

[108] Umemoto Y, Sugawara K, Nakata Y, Takahashi T and Sato T 2019 Pseudogap, Fermi arc, and Peierls-insulating phase induced by 3D2D crossover in monolayer VSe$_2$ *Nano Res.* **12** 1659

[109] Zong J *et al.* 2022 Observation of multiple charge density wave phases in epitaxial monolayer 1T-VSe$_2$ film *Chin. Phys. B* **31** 107301

[110] Chen P, Chan Y-H, Liu R-Y, Zhang H T, Gao Q, Fedorov A-V, Chou M Y and Chiang T-C 2022 Dimensional crossover and symmetry transformation of charge density waves in VSe$_2$ *Phys. Rev. B* **105** L161404

[111] Jang I, Duvjir G, Choi B K, Kim J, Chang Y J and Kim K-S 2019 Universal renormalization group flow toward perfect Fermi-surface nesting driven by enhanced electron-electron correlations in monolayer vanadium diselenide *Phys. Rev. B* **99** 014106

[112] Sugawara K, Nakata Y, Fujii K, Nakayama K, Souma S, Takahashi T and Sato T 2019 Monolayer VTe$_2$: Incommensurate Fermi surface nesting and suppression of charge density waves *Phys. Rev. B* **99** 241404

[113] Wang Y, Ren J, Li J, Wang Y, Peng H, Yu P, Duan W and Zhou S 2019 Evidence of charge density wave with anisotropic gap in a monolayer VTe$_2$ *Phys. Rev. B* **100** 241404

[114] Coelho P M, Lasek K, Cong K N, Li J, Niu W, Liu W, Oleynik I I and Batzill M 2019 Monolayer modification of VTe$_2$ and its charge density wave *J. Phys. Chem. Lett.* **10** 498793

[115] Whangbo M H and Canadell E 1992 Analogies between the concepts of molecular chemistry and solid-state physics concerning structural instabilities. Electronic origin of the structural modulations in layered transition metal dichalcogenides *J. Am. Chem. Soc.* **114** 9587600

[116] Jobic S, Brec R and Rouxel J 1992 Anionic polymeric bonds in transition metal ditellurides *J. Solid State Chem.* **96** 16980

[117] Mitsuishi N *et al.* 2020 Switching of band inversion and topological surface states by charge density wave *Nat. Commun.* **11** 2466

[118] Di Salvo F J *et al.* 1976 Electronic properties and superlattice formation in the semimetal TiSe$_2$ *Phys. Rev. B* **14** 4321-4328

[119] Porer M, Leierseder U, Mnard J M, Dachraoui H, Mouchliadis L, Perakis I E, Heinzmann U, Demsar J, Rossnagel K and Huber R 2014 Non-thermal separation of electronic and structural orders in a persisting charge density wave *Nat. Mater.* **13** 85761

[120] Kogar A *et al.* 2017 Signatures of exciton condensation in a transition metal dichalcogenide *Science* **358** 13147

[121] Mor S, Herzog M, Monney C and Sthler J 2022 Ultrafast charge carrier and exciton dynamics in an excitonic insulator probed by time-resolved photoemission spectroscopy *Prog. Surf. Sci.* **97** 100679

[122] Chen P, Chan Y H, Fang X Y, Zhang Y, Chou M Y, Mo S-K, Hussain Z, Fedorov A V and Chiang T-C 2015 Charge density wave transition in single-layer titanium diselenide *Nat. Commun.* **6** 8943

[123] Sugawara K, Nakata Y, Shimizu R, Han P, Hitosugi T, Sato T and Takahashi T 2016 Unconventional charge-density-wave transition in monolayer 1T-TiSe$_2$ *ACS Nano* **10** 13415

[124] Chen P, Chan Y H, Fang X Y, Mo S-K, Hussain Z, Fedorov A V, Chou M Y and Chiang T-C 2016 Hidden Order and Dimensional Crossover of the Charge Density Waves in TiSe$_2$ *Sci. Rep.* **6** 37910

[125] Chen P, Chan Y H, Wong M H, Fang X Y, Chou M Y, Mo S-K, Hussain Z, Fedorov A V and Chiang T-C 2016 Dimensional Effects on the Charge Density Waves in Ultrathin Films of TiSe$_2$ *Nano Lett.* **16** 63316

[126] Hsu M-C, Singh B, Hsu C-H, Xu S-Y, Lin H and Huang S-M 2021 Topological theory of inversion-breaking charge-density-wave monolayer 1T-TiSe$_2$ *N. J. Phys.* **23** 093025

[127] Singh B, Hsu C-H, Tsai W-F, Pereira V M and Lin H 2017 Stable charge density wave phase in a 1TTiSe$_2$ monolayer *Phys. Rev. B* **95** 245136

[128] Mulani I, Rajput U, Harnagea L and Deshpande A 2021 Perturbation of charge density waves in 1T-TiSe$_2$ *Phys. Rev. B* **103** 125430

[129] Watson M D *et al.* 2021 Strong-coupling charge density wave in monolayer TiSe$_2$ *2D Mater.* **8** 015004

[130] Li L J, Zhao W J, Liu B, Ren T H, Eda G and Loh K P 2016 Enhancing charge-density-wave order in 1T-TiSe$_2$ nanosheet by encapsulation with hexagonal boron nitride *Appl. Phys. Lett.* **109** 141902

[131] Kolekar S, Bonilla M, Ma Y, Diaz H C and Batzill M 2017 Layer- and substrate-dependent charge density wave criticality in 1TTiSe$_2$ *2D Mater.* **5** 015006

[132] Kolekar S, Bonilla M, Diaz H C, Hashimoto M, Lu D and Batzill M 2018 Controlling the charge density wave transition in monolayer TiSe$_2$: substrate and doping effects *Adv. Quantum Technol.* **1** 1800070

[133] Chernikov A, Berkelbach T C, Hill H M, Rigosi A, Li Y, Aslan O B, Reichman D R, Hybertsen M S and Heinz T F 2014 Exciton binding energy and nonhydrogenic Rydberg series in monolayer WS$_2$ *Phys. Rev. Lett.* **113** 076802

[134] Qiu D Y, Jornada F H da and Louie S G 2016 Screening and many-body effects in two-dimensional crystals: Monolayer MoS$_2$ *Phys. Rev. B* **93** 235435

[135] Ugeda M M *et al.* 2014 Giant bandgap renormalization and excitonic effects in a monolayer transition metal dichalcogenide semiconductor. *Nat. Mater.* **13** 10915

[136] Chen P *et al.* 2017 Emergence of charge density waves and a pseudogap in single-layer TiTe$_2$ *Nat. Commun.* **8** 516

[137] Fragkos S, Sant R, Alvarez C, Bosak A, Tsipas P, Tsoutsou D, Okuno H, Renaud G and Dimoulas A 2019 Room temperature commensurate charge density wave in epitaxial strained TiTe$_2$ multilayer films *Adv. Mater. Interfaces* **6** 1801850

[138] Lin M-K, Hlevyack J A, Chen P, Liu R-Y, Mo S-K and Chiang T-C 2020 Charge instability in single-layer TiTe$_2$ mediated by van der Waals bonding to substrates *Phys. Rev. Lett.* **125** 176405

[139] Antonelli T *et al.* 2022 Orbital-selective band hybridisation at the charge density wave transition in monolayer TiTe$_2$ *npj Quantum Mater.* **7** 98

[140] Zhao W-M, Zhu L, Nie Z, Li Q-Y, Wang Q-W, Dou L-G, Hu J-G, Xian L, Meng S and Li S-C 2022 Moir enhanced charge density wave state in twisted 1T-TiTe$_2$/1T-TiSe$_2$ heterostructures *Nat Mater* **21** 2849

[141] Ishiguro T *et al.* 1991 Electron microscopy of phase transformations in 1T-TaS$_2$ *Phys. Rev. B* **44** 2046-2060

[142] Tosatti E and Fazekas P 1979 Electrical, structural and magnetic properties of pure and doped 1T-TaS$_2$ *Phil. Mag. B* **39** 229-244

[143] Thompson A, Gamble R and Revelli J 1971 Transitions between semiconducting and metallic phases in 1T-TaS$_2$, *Solid State Communications* **9** 981-985

[144] Perfetti L, Georges A, Florens S, Biermann S, Mitrovic S, Berger H, Tomm Y, Hochst H and Grioni M 2003, Spectroscopic signatures of a bandwidth-controlled Mott transition at the surface of 1T-TaSe$_2$ *Phys. Rev. Lett.* **90** 166401

[145] Colonna S, Ronci F, Cricenti A, Perfetti L, Berger H and Grioni M 2005, Mott phase at the surface of 1T-TaSe$_2$ observed by scanning tunneling microscopy *Phys. Rev. Lett.* **94** 036405

[146] Tosatti E and Fazekas P 1976 On the nature of the low-temperature phase of 1T-TaS$_2$ *J. phys., Colloq.* **37** C4-165

[147] Mott N F 1968 Metal-insulator transition *Rev. Mod. Phys.* **40** 677-683

[148] Imada M, Fujimori A. and Tokura Y. 1998 Metal-insulator transitions *Rev. Mod. Phys.* **70** 1039-1263

[149] Darancet P, Millis A J and Marianetti C A 2014 Three-dimensional metallic and two-dimensional insulating behavior in octahedral tantalum dichalcogenides *Phys. Rev. B* **90** 045134

[150] Yu X-L, Liu D-Y, Quan Y-M, Wu J, Lin H-Q, Chang K and Zou L-J 2017 Electronic correlation effects and orbital density wave in the layered compound 1T-TaS$_2$ *Phys. Rev. B* **96** 125138

[151] Yi S, Zhang Z and Cho J-H 2018 Coupling of charge, lattice, orbital, and spin degrees of freedom in charge density waves in 1T-Tas$_2$ *Phys. Rev. B* **97** 041413

[152] Chen Y *et al.* 2020 Strong correlations and orbital texture in single-layer 1T-TaSe$_2$ *Nat. Phys.* **16** 21824

[153] Law K T and Lee P A 2017 1T-TaS$_2$ as a quantum spin liquid *Proc. Natl. Acad. Sci. U.S.A* **114** 6996-7000

[154] He W Y, Xu X Y, Chen G, Law K T and Lee P A 2018 Spinon Fermi surface in a cluster Mott insulator model on a triangular lattice and possible application to 1T-TaS$_2$ *Phys. Rev. Lett.* **121** 046401

[155] Klanjek M, Zorko A, itko R, Mravlje J, Jaglii Z, Biswas P K, Prelovek P, Mihailovic D and Aron D 2017 A high-temperature quantum spin liquid with polaron spins *Nat. Phys.* **13** 11304

[156] Kratochvilova M, Hillier A D, Wildes A R, Wang L, Cheong S-W and Park J-G 2017 The low-temperature highly correlated quantum phase in the charge-density-wave 1T-TaS$_2$ compound *npj Quant. Mater.* **2** 42

[157] Ribak A, Silber I, Baines C, Chashka K, Salman Z, Dagan Y and Kanigel A 2017 Gapless excitations in the ground state of 1T-TaS$_2$ *Phys. Rev. B* **96** 195131

[158] Ritschel T, Trinckauf J, Koepernik K, Bchner B, Zimmermann M v, Berger H, Joe Y I, Abbamonte P and Geck J 2015 Orbital textures and charge density waves in transition metal dichalcogenides *Nat. Phys.* **11** 328-331

[159] Ritschel T, Berger H and Geck J 2018 Stacking-driven gap formation in layered 1T-TaS$_2$ *Phys. Rev. B* **98** 195134

[160] Lee S-H, Goh J S and Cho D 2019 Origin of the Insulating Phase and First-Order Metal-Insulator Transition in 1T-TaS$_2$ *Phys. Rev. Lett.* **122** 106404

[161] Nakanishi K and Shiba H 1984 Theory of three-dimensional orderings of charge-density waves in 1T-TaX$_2$ (X: S, Se) *J. Phys. Soc. Jpn.* **53** 1103-1113

[162] von Witte G, Kilinger T, Horstmann J G, Rossnagel K, Schneider M A, Ropers C and Hammer L 2019 Surface structure and stacking of the commensurate $(\sqrt{13} \times \sqrt{13})R13.9°$ charge density wave phase of 1T-TaS$_2$ *Phys. Rev. B* **100** 155407

[163] Stahl Q, Kusch M, Heinsch F, Garbarino G, Kretzschmar N, Hanff K, Rossnagel K, Geck J and Ritschel T 2020 Collapse of layer dimerization in the photo-induced hidden state of 1T-TaS$_2$ *Nat. Commun.* **11** 1247

[164] Wang Y D, Yao W L, Xin Z M, Han T T, Wang Z G, Chen L, Cai C, Li Y and Zhang Y 2020 Band insulator to Mott insulator transition in 1T-TaS$_2$ *Nat. Commun.* **11** 4215

[165] Petocchi F, Nicholson C W, Salzmann B, Pasquier D, Yazyev O V, Monney C and Werner P 2022 Mott versus hybridization gap in the low-temperature phase of 1T-TaS$_2$ *Phys. Rev. Lett.* **129** 016402

[166] Butler C J, Yoshida M, Hanaguri T and Iwasa Y 2020 Mottness versus unit-cell doubling as the driver of the insulating state in 1T-TaS$_2$ *Nat. Commun.* **11** 2477

[167] Butler C J, Yoshida M, Hanaguri T and Iwasa Y 2021 Doublonlike excitations and their phononic coupling in a Mott charge-density-wave system *Phys. Rev. X* **11** 011059

[168] Yao Q, Park J W, Oh E and Yeom H W 2021 Engineering domain wall electronic states in strongly correlated van der Waals material of 1T-TaS$_2$ *Nano Lett.* **21** 9699-9705

[169] Wu Z, Bu K, Zhang W, Fei Y, Zheng Y, Gao J, Luo X, Liu Z, Sun Y-P and Yin Y 2022 Effect of stacking order on the electronic state of 1T-TaS$_2$ *Phys. Rev. B* **105** 035109

[170] Zhang W, Wu Z, Bu K, Fei Y, Zheng Y, Gao J, Luo X, Liu Z, Sun Y-P and Yin Y 2022 Reconciling the bulk metallic and surface insulating state in 1T-TaSe$_2$ *Phys. Rev. B* **105** 035110

[171] Chen Y, Ruan W, Cain J D, Lee R L, Kahn S, Jia C, Zettl A and Crommie M F 2022 Observation of a multitude of correlated states at the surface of bulk 1T-TaSe$_2$ crystals *Phys. Rev. B* **106** 075153

[172] Lee J, Jin K-H and Yeom H W 2021 Distinguishing a Mott insulator from a trivial insulator with atomic adsorbates *Phys. Rev. Lett.* **126** 196405

[173] Zhu X-Y *et al.* 2019 Realization of a metallic state in 1T-TaS$_2$ with persisting long-range order

of a charge density wave *Phys. Rev. Lett.* **123** 206405

[174] Zhang W *et al.* 2022 Modulation of electronic state in copper-intercalated 1T-TaS$_2$ *Nano Res.* **15** 4327-4333

[175] Zhang W *et al.* 2022 Visualizing the evolution from Mott insulator to Anderson insulator in Ti-doped 1T-TaS$_2$ *npj Quantum Mater.* **7** 8

[176] Jung J, Jin K-H, Kim J and Yeom H W 2023 Control over a wide phase diagram of 2D correlated electrons by surface doping; K/1T-TaS$_2$ *Nano Lett.* **23** 8029-8034

[177] Ma L *et al.* 2016 A metallic mosaic phase and the origin of Mott-insulating state in 1T-TaS$_2$ *Nat. Commun.* **7** 10956

[178] Cho D, Cheon S, Kim K-S, Lee S-H, Cho Y-H, Cheong S-W and Yeom H W 2016 Nanoscale manipulation of the Mott insulating state coupled to charge order in 1T-TaS$_2$ *Nat. Commun.* **7** 10453

[179] Cho D, Gye G, Lee J, Lee S-H, Wang L, Cheong S-W and Yeom H W 2017 Correlated electronic states at domain walls of a Mott-charge-density-wave insulator 1T-TaS$_2$ *Nat. Commun.* **8** 392

[180] Skolimowski J, Gerasimenko Y and itko R 2019 Mottness collapse without metallization in the domain wall of the triangular-lattice Mott insulator 1T-TaS$_2$ *Phys. Rev. Lett.* **122** 036802

[181] Aishwarya A, Raghavan A, Howard S, Cai Z, Thakur G S, Won C, Cheong S-W, Felser C and Madhavan V 2022 Long-lifetime spin excitations near domain walls in 1T-TaS$_2$ *Proc. Natl. Acad. Sci.* **119** e2121740119

[182] Hellmann S *et al.* 2012 Time-domain classification of charge-density-wave insulators *Nat. Commun.* **3** 1069

[183] Sohrt C, Stange A, Bauer M and Rossnagel K 2014 How fast can a PeierlsMott insulator be melted? *Faraday Discuss.* **171** 243-257

[184] Petersen J C *et al.* 2011 Clocking the melting transition of charge and lattice order in 1T-TaS$_2$ with ultrafast extreme-ultraviolet angle-resolved photoemission spectroscopy *Phys. Rev. Lett.* **107** 177402

[185] Ligges M *et al.* 2018 Ultrafast doublon dynamics in photoexcited 1T-TaS$_2$ *Phys. Rev. Lett.* **120** 166401

[186] Stojchevska L, Vaskivskyi I, Mertelj T, Kusar P, Svetin D, Brazovskii S and Mihailovi D 2014 Ultrafast switching to a stable hidden quantum state in an electronic crystal *Science* **344** 177-180

[187] Vaskivskyi I, Gospodaric J, Brazovskii S, Svetin D, Sutar P, Goreshnik E, Mihailovic I A, Mertelj T and Mihailovic D 2015 Controlling the metal-to-insulator relaxation of the metastable hidden quantum state in 1T-TaS$_2$ *Sci. Adv.* **1** e1500168

[188] Fei Y, Wu Z, Zhang W and Yin Y 2022 Understanding the Mott insulating state in 1T-TaS$_2$ and 1T-TaSe$_2$ *AAPPS Bulletin* **32** 20

[189] Nakata Y, Sugawara K, Shimizu R, Okada Y, Han P, Hitosugi T, Ueno K, Sato T and Takahashi T 2016 Monolayer 1T-NbSe$_2$ as a Mott insulator *NPG Asia Mater.* **8** e321

[190] Lin H, Huang W, Zhao K, Lian C, Duan W, Chen X and Ji S-H 2018 Growth of atomically thick transition metal sulfide films on graphene/6H-SiC(0001) by molecular beam epitaxy *Nano Res.* **11** 4722-4727

[191] Nakata Y, Yoshizawa T, Sugawara K, Umemoto Y, Takahashi T and Sato T 2018 Selective fabrication of Mott-insulating and metallic monolayer TaSe$_2$ *ACS Appl. Nano Mater.* **1** 1456-1460

[192] Liu M *et al.* 2021 Monolayer 1T-NbSe$_2$ as a 2D-correlated magnetic insulator *Sci. Adv.* **7** eabi6339

[193] Lin H, Huang W, Zhao K, Qiao S, Liu Z, Wu J, Chen X and Ji S-H 2020 Scanning tunneling spectroscopic study of monolayer 1*T*-TaS$_2$ and 1*T*-TaSe$_2$ *Nano Res.* **13** 133-137

[194] Ruan W *et al.* 2021 Evidence for quantum spin liquid behaviour in single-layer 1*T*-TaSe$_2$ from scanning tunnelling microscopy *Nat. Phys.* **17** 115461

[195] Vao V, Amini M, Ganguli S C, Chen G, Lado J L, Kezilebieke S and Liljeroth P 2021 Artificial heavy fermions in a van der Waals heterostructure *Nature* **599** 5826

[196] Liu L *et al.* 2021 Direct identification of Mott Hubbard band pattern beyond charge density wave superlattice in monolayer 1T-NbSe$_2$ *Nat. Commun.* **12** 1978

[197] Zhang Q *et al.* 2023 Quantum spin liquid signatures in monolayer 1T-NbSe$_2$ preprint. DOI:10.21203/rs.3.rs-3247091/v1

[198] Tian N *et al.* 2024 Dimensionality-driven metal to Mott insulator transition in two-dimensional 1T-TaSe$_2$ *Natl. Sci. Rev.* **11** nwad144

[199] Wang Y D, Yao W L, Xin Z M, Han T T, Wang Z G, Chen L, Cai C, Li Y and Zhang Y 2020 Band insulator to Mott insulator transition in 1T-TaS$_2$ *Nat. Commun.* **11** 4215

[200] Motrunich O I 2005 Variational study of triangular lattice spin-1/2 model with ring exchanges and spin liquid state in κ-(ET)$_2$Cu$_2$(CN)$_3$ *Phys. Rev. B* **72** 045105

[201] Lee S-S and Lee P A 2005 U(1) gauge theory of the Hubbard model: spin liquid states and possible application to κ-(BEDT-TTF)$_2$Cu$_2$(CN)$_3$ *Phys. Rev. Lett.* **95** 036403

[202] Wen X-G 2002 Quantum orders and symmetric spin liquids *Phys. Rev. B* **65** 165113

[203] Lee P A 2008 An end to the drought of quantum spin liquids *Science* **321** 13067

[204] Balents L 2010 Spin liquids in frustrated magnets *Nature* **464** 199208

[205] Zhou Y, Kanoda K and Ng T-K 2017 Quantum spin liquid states *Rev. Mod. Phys.* **89** 025003

[206] Wen J, Yu S-L, Li S, Yu W and Li J-X 2019 Experimental identification of quantum spin liquids *npj Quantum Mater.* **4** 12

[207] Yu Y J, Xu Y, He L P, Kratochvilova M, Huang Y Y, Ni J M, Wang L, Cheong S-W, Park J-G and Li S Y 2017 Heat transport study of the spin liquid candidate 1T-TaS$_2$ *Phys. Rev. B* **96** 081111

[208] Chen C, Sodemann I and Lee P A 2021 Competition of spinon Fermi surface and heavy Fermi liquid states from the periodic Anderson to the Hubbard model *Phys. Rev. B* **103** 085128

[209] Norman M R and Micklitz T 2009 How to measure a spinon Fermi surface *Phys. Rev. Lett.* **102** 067204

[210] Mross D F and Senthil T 2011 Charge Friedel oscillations in a Mott insulator *Phys. Rev. B* **84** 041102

[211] Ribeiro P and Lee P A 2011 Magnetic impurity in a U(1) spin liquid with a spinon Fermi surface *Phys. Rev. B* **83** 235119

[212] Chen Y *et al.* 2022 Evidence for a spinon Kondo effect in cobalt atoms on single-layer 1*T*-TaSe$_2$ *Nat. Phys.* **18** 133540

[213] Agterberg D F and Tsunetsugu H 2008 Dislocations and vortices in pair-density-wave superconductors *Nat. Phys.* **4** 63942

[214] Fradkin E, Kivelson S A and Tranquada J M 2015 Colloquium: Theory of intertwined orders in high temperature superconductors *Rev. Mod. Phys.* **87** 45782

[215] Gomilek M, itko R, Klanjek M, Pregelj M, Baines C, Li Y, Zhang Q M and Zorko A 2019 Kondo screening in a charge-insulating spinon metal *Nat. Phys.* **15** 7548

[216] He W-Y and Lee P A 2022 Magnetic impurity as a local probe of the U(1) quantum spin liquid with spinon Fermi surface *Phys. Rev. B* **105** 195156

[217] Rodriguez J P and Lederer P 1996 Confinement of spin and charge in high-temperature superconductors *Phys. Rev. B* **53** R119803

[218] Cercellier H *et al.* 2007 Evidence for an excitonic insulator phase in 1T-TiSe$_2$ *Phys. Rev. Lett.* **99** 146403

[219] Monney G, Monney C, Hildebrand B, Aebi P and Beck H 2015 Impact of electron-hole correlations on the 1T-TiSe$_2$ electronic structure *Phys. Rev. Lett.* **114** 086402

[220] Sun B *et al.* 2022 Evidence for equilibrium exciton condensation in monolayer WTe$_2$ *Nat. Phys.* **18** 949

[221] Jia Y *et al.* 2022 Evidence for a monolayer excitonic insulator *Nat. Phys.* **18** 8793

[222] Wakisaka Y, Sudayama T, Takubo K, Mizokawa T, Arita M, Namatame H, Taniguchi M, Katayama N, Nohara M and Takagi H 2009 Excitonic insulator state in Ta$_2$NiSe$_5$ probed by photoemission spectroscopy *Phys. Rev. Lett.* **103** 026402

[223] Fukutani K, Stania R, Kwon C I, Kim J S, Kong K J, Kim J and Yeom H W 2021 Detecting photoelectrons from spontaneously formed excitons *Nat. Phys.* **17** 102430

[224] Chen C *et al.* 2023 Role of electron-phonon coupling in excitonic insulator candidate Ta2NiSe5 *Phys. Rev. Res.* **5** 043089

[225] Song Y *et al.* 2023 Signatures of the exciton gas phase and its condensation in monolayer 1T-ZrTe$_2$ *Nat. Commun.* **14** 1116

[226] Gao Q *et al.* 2023 Evidence of high-temperature exciton condensation in a two-dimensional semimetal *Nat. Commun.* **14** 994

[227] Ren M-Q *et al.* 2022 Semiconductormetal phase transition and emergent charge density waves in 1TZrX$_2$ (X = Se, Te) at the two-dimensional limit *Nano Lett.* **22** 47684

[228] Yang L-N, Xu Y-J, Li Q-Y, Meng Y-X, Zhao Y-F and Li S-C 2022 Coexistence of the charge density wave state and linearly dispersed energy band in 1T-ZrTe$_2$ monolayer *Appl. Phys. Lett.* **120** 073105

[229] Tsipas P, Tsoutsou D, Fragkos S, Sant R, Alvarez C, Okuno H, Renaud G, Alcotte R, Baron T and Dimoulas A 2018 Massless Dirac fermions in ZrTe$_2$ semimetal grown on InAs(111) by van der Waals epitaxy *ACS Nano* **12** 1696703

[230] Canadell E, Jobic S, Brec R, Rouxel J and Whangbo M-H 1992 Importance of short interlayer TeTe contacts for the structural distortions and physical properties of CdI$_2$-type layered transition-metal ditellurides *J. Solid State Chem.* **99** 18999

[231] Yoshida M, Kudo K, Nohara M and Iwasa Y 2018 Metastable superconductivity in two-dimensional IrTe$_2$ crystals *Nano Lett.* **18** 31137

[232] Li J *et al.* 2018 Synthesis of ultrathin metallic MTe$_2$ (M = V, Nb, Ta) singlecrystalline nanoplates *Adv. Mater.* **30** 1801043

[233] Zhou R, Zhao Z, Wu J and Xie L 2020 Chemical vapor deposition of IrTe$_2$ thin films *Crystals* **10** 575

[234] Jobic S, Deniard P, Brec R, Rouxel J, Jouanneaux A and Fitch A N 1991 Crystal and electronic band structure of IrTe$_2$: Evidence of anionic bonds in a CdI$_2$like arrangement *Z. fr Anorg. Allg. Chem.* **598** 199215

[235] Ko K T *et al.* 2015 Charge-ordering cascade with spin-orbit Mott dimer states in metallic iridium ditelluride *Nat. Commun.* **6** 7342

[236] Kim K, Kim S, Ko K T, Lee H, Park J H, Yang J J, Cheong S W and Min B I 2015 Origin of first-order-type electronic and structural transitions in IrTe$_2$ *Phys. Rev. Lett.* **114** 136401

[237] Pascut G L *et al.* 2013 Dimerization-induced cross-layer quasi-two-dimensionality in metallic IrTe$_2$ *Phys. Rev. Lett.* **112** 086402

[238] Dai J, Haule K, Yang J J, Oh Y S, Cheong S-W and Wu W 2014 Hierarchical stripe phases in IrTe$_2$ driven by competition between Ir dimerization and Te bonding *Phys. Rev. B* **90** 235121

[239] Oh Y S, Yang J J, Horibe Y and Cheong S-W 2013 Anionic depolymerization transition in IrTe$_2$ *Phys. Rev. Lett.* **110** 127209

[240] Hwang J *et al.* 2022 Large-gap insulating dimer ground state in monolayer IrTe$_2$ *Nat. Commun.* **13** 906

[241] Streltsov S V and Khomskii D I 2017 Orbital physics in transition metal compounds: new trends *Phys.-Usp.* **60** 112146

[242] Bozin E S, Yin W G, Koch R J, Abeykoon M, Hor Y S, Zheng H, Lei H C, Petrovic C, Mitchell J F and Billinge S J L 2019 Local orbital degeneracy lifting as a precursor to an orbital-selective Peierls transition *Nat. Commun.* **10** 3638

[243] Hwang J *et al.* 2022 A novel $\sqrt{19}$ $\sqrt{19}$ superstructure in epitaxially grown 1TTaTe$_2$ *Adv. Mater.* **34** 2204579

[244] Bernardo I D, RipollSau J, SilvaGuilln J A, Calleja F, Ayani C G, Miranda R, Canadell E, Garnica M and Parga A L V de 2023 Metastable polymorphic phases in monolayer TaTe$_2$ *Small* **2023** 2300262

[245] Bai Y *et al.* 2023 Realization of multiple charge-density waves in NbTe$_2$ at the monolayer limit *Nano Lett.* **23** 210713

[246] Yumigeta K, Qin Y, Li H, Blei M, Attarde Y, Kopas C and Tongay S 2021 Advances in rareearth

tritelluride quantum materials: structure, properties, and synthesis *Adv. Sci.* **8** 2004762

[247] Dumas J and Schlenker C 1993 Charge Density Wave Properties Of Molybdenum Bronzes *Int. J. Mod. Phys. B* **7** 4045108

[248] Miao H *et al.* 2019 Formation of incommensurate charge density waves in cuprates *Phys. Rev. X* **9** 031042

[249] Miao H *et al.* 2021 Charge density waves in cuprate superconductors beyond the critical doping *npj Quantum Mater.* **6** 31

[250] Božović I, He X, Wu J and Bollinger A T 2016 Dependence of the critical temperature in overdoped copper oxides on superfluid density *Nature 536* 309

[251] Zhong Y, Chen Z, Chen S-D, Xu K-J, Hashimoto M, He Y, Uchida S, Lu D, Mo S-K and Shen Z-X 2022 Differentiated roles of Lifshitz transition on thermodynamics and superconductivity in $La_{2-x}Sr_xCuO_4$ *Proc. National. Acad. Sci.* **119** e2204630119

[252] Lander G H, Fisher E S and Bader S D 1994 The solid-state properties of uranium: A historical perspective and review *Adv. Phys.* **43** 1111

[253] Springell R, Bright E L, Chaney D A, Harding L M, Bell C, Ward R C C and Lander G H 2022 A review of uranium-based thin films *Adv. Phys.* **71** 87165

[254] Cheng S, Wang B, Lyalin I, Bagus N, Bishop A J, McComb D W and Kawakami R K 2022 Atomic layer epitaxy of kagome magnet Fe_3Sn_2 and Sn-modulated heterostructures *APL Mater.* **10** 061112

[255] Zhang H, Weinert M and Li L 2023 Giant periodic pseudomagnetic fields in strained kagome magnet FeSn epitaxial films on $SrTiO_3(111)$ substrate *Nano Lett.* **23** 2397404

[256] Novoselov K S, Mishchenko A, Carvalho A and Neto A H C 2016 2D materials and van der Waals heterostructures *Science* **353** 461461

[257] Andrei E Y and MacDonald A H 2020 Graphene bilayers with a twist *Nat. Mater.* **19** 126575